JGR Oceans

RESEARCH ARTICLE
10.1029/2022JC018648

Summer Hydrography and Circulation in Storfjorden, Svalbard, Following a Record Low Winter Sea-Ice Extent in the Barents Sea

Frédéric Vivier[1], Antonio Lourenço[1], Elisabeth Michel[2], Ragnheid Skogseth[3], Clément Rousset[1], Bruno Lansard[2], Pascale Bouruet-Aubertot[1], Jacqueline Boutin[1], Bruno Bombled[2], Yannis Cuypers[1], Olivier Crispi[4], Dennis Dausse[1], Hervé Le Goff[1], Gurvan Madec[1], Martin Vancoppenolle[1], Fanny Van der Linden[5], and Claire Waelbroeck[1]

[1]LOCEAN-IPSL, CNRS, Sorbonne Université, Paris, France, [2]LSCE, CEA-CNRS-UVSQ, Université Paris-Saclay—IPSL, Gif sur Yvette, France, [3]The University Centre in Svalbard, Longyearbyen, Norway, [4]LOMIC, Observatoire Océanologique de Banyuls sur Mer, Banyuls sur Mer, France, [5]Unité d'Océanographie Chimique, Université de Liège, Liège, Belgium

Abstract Storfjorden, Svalbard, hosts a polynya in winter and is an important source region of Brine-enriched Shelf Water (BSW) that, if dense enough, feeds the Arctic Ocean deep water reservoir. Changes in the BSW production may thus have far-reaching impacts. We analyze the water mass distribution and circulation in Storfjorden and the trough south of it, Storfjordrenna, using hydrographic sections occupied in July 2016, following a winter characterized by the lowest ice coverage recorded in the Barents Sea. These observations reveal an unusual hydrographic state, characterized at the surface by the near absence of Melt Water and Storfjorden Surface Water, replaced by a saltier water mass. At depth, BSW (maximum salinity of 34.95) was found from the bottom up to 90 m, above the 120-m deep sill at the mouth to Storfjordrenna. However, no gravity driven overflow was observed downstream of the sill: the dome of BSW remained locked over the depression in a cyclonic circulation pattern consistent with a stratified Taylor column. Observations further reveal a previously unreported intrusion of Atlantic Water (AW) far into the fjord, promoting isopycnal mixing with entrapped Arctic Water. This intrusion was possibly favored by positive wind stress curl anomalies over Svalbardbanken and Storfjordrenna. The bottom plume exiting Storfjordrenna was weak, carrying Polar Front Water rather than BSW, too light to sink underneath the AW layer at Fram Strait. Whether Storfjorden switched durably to a new hydrographic state, following the observed Atlantification of the Barents Sea after 2005, remains to be established.

Plain Language Summary Storfjorden, east of Spitsbergen, plays an important role in Arctic Ocean climate through formation of dense water as salt is added to the ocean when sea ice forms. This dense water accumulates in winter before spilling toward the deep ocean into autumn, fueling the global ocean's circulation. We analyze observations from a research cruise in July 2016, following a winter season characterized by the lowest ice coverage in the Barents Sea ever recorded. These observations reveal striking differences from previous reports, which are mostly based on data prior to the 2005 regime shift in the Barents Sea characterized by warmer temperature and reduced ice cover, an expression of its "Atlantification" reported by many authors. First, the expected overflow of the locally formed dense water was absent. The latter, less saline than usual, was instead trapped in Storfjorden suggesting an intermittent discharge regime usually observed in the fall. Another notable observation is the intrusion of Atlantic Water far inside the fjord. Such a flooding episode, increasingly frequent in the fjords of the west coast of Spitsbergen, is previously unreported in Storfjorden. These observations made in the wake of an exceptionally mild winter could prefigure more permanent changes in this important region.

Key Points:

- Changes in the hydrography and circulation in Storfjorden a decade after a regime shift in the Barents Sea linked to its Atlantification
- The less saline Brine-enriched Shelf Water remained entrapped in Storfjorden within a cyclonic circulation pattern with no overflow
- Storfjorden was flooded with Atlantic Water, promoting isopycnal mixing with Arctic Water and the local formation of East Spitsbergen Water

Supporting Information:

Supporting Information may be found in the online version of this article.

Correspondence to:

F. Vivier,
frederic.vivier@locean.ipsl.fr

Citation:

Vivier, F., Lourenço, A., Michel, E., Skogseth, R., Rousset, C., Lansard, B., et al. (2023). Summer hydrography and circulation in Storfjorden, Svalbard, following a record low winter sea-ice extent in the Barents Sea. *Journal of Geophysical Research: Oceans*, *128*, e2022JC018648. https://doi.org/10.1029/2022JC018648

Received 22 MAR 2022
Accepted 26 JAN 2023

1. Introduction

It has been known since the 1980's that continental shelves must contribute substantially to the formation of Arctic Ocean deep waters through the sinking of dense Brine-enriched Shelf Water (BSW) (Aagaard, 1981; Aagaard et al., 1985; Rudels, 1986; Rudels & Quadfasel, 1991; Swift et al., 1983). The initial intuition that shelf water enriched with brine during freezing could ventilate the deep layers of the Arctic Ocean can be traced back to Nansen (1906) based on observations from several expeditions of the early twentieth century. In the modern era these inferences were first confirmed by observations of the spreading of dense plumes of BSW on the shelf of

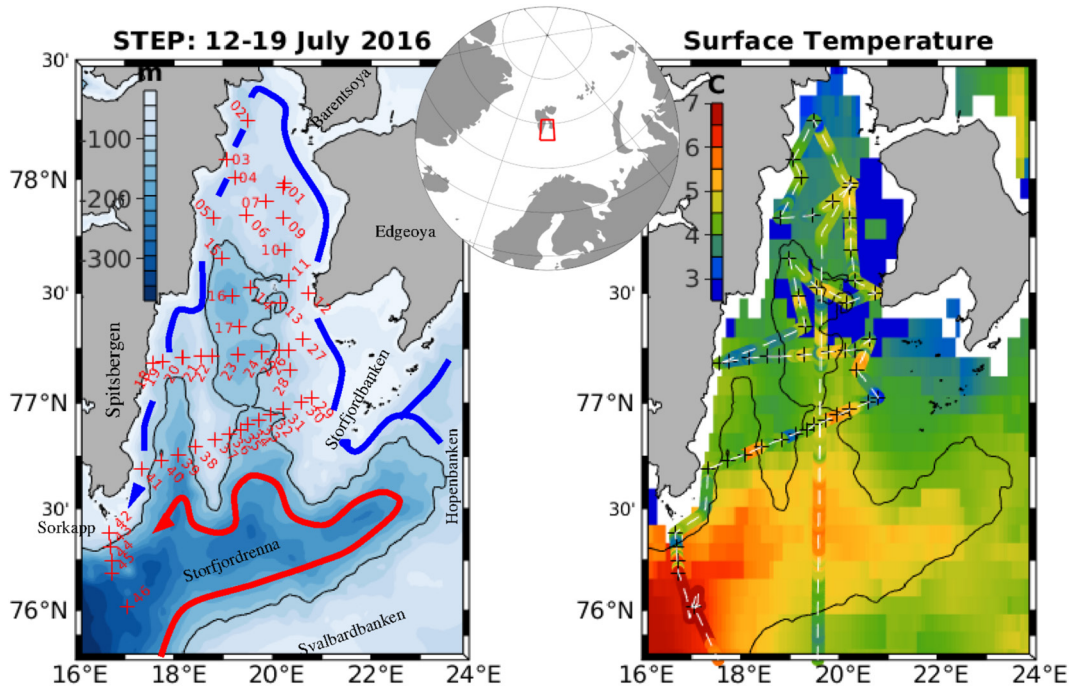

Figure 1. Map of the STEP 2016 cruise. Left: Hydrographic stations superimposed on the ETOPO1 bathymetry. The 120 m isobath, that marks the sill at the entrance of Storfjorden, is indicated. The branch of the NAC flowing into Storfjordrenna and the cyclonic costal current around Storfjorden are sketched. Right: satellite Sea Surface Temperature (SST) image of 19 July 2016 with superimposition of the near-surface temperature from the ship's thermosalinograph between 12 and 19 July. Satellite SST is a merged infrared-microwave product from Remote Sensing Systems.

Novaya Zemlya and the Svalbard bank (Midttun, 1985) or, in 1986, on the continental slope of Svalbard at Fram Strait down to depths of more than 2,000 m (Quadfasel et al., 1988). The latter plume was estimated to contribute 5%–10% of the annual deep water production of the polar basins and its origin was traced to Storfjorden where a particularly saline BSW (>35.4) had been observed in 1986 (Anderson et al., 1988). These observations have fostered dedicated surveys with current meter moorings (Bensi et al., 2019; Sanchez-Vidal et al., 2015; Schauer, 1995; Schauer & Fahrbach, 1999) or hydrographic sections (e.g., Fer et al., 2003) and several numerical studies on the plume dynamics and mixing along the path from the sill to the shelf-slope in the Fram Strait (Fer & Ådlandsvik, 2008; Jungclaus et al., 1995; Wobus et al., 2013). Deep-reaching slope convection generating a plume sinking along the continental slope into Fram Strait is not a regular feature and was only reported twice, in 1988 and 2002, since its original observation in 1986 (Akimova et al., 2011). Whether the Storfjorden plume descends into the deep ocean or, instead, interleaves with ambient waters at shallower depth depends on the salinity of the BSW formed in Storfjorden during wintertime: this varies substantially from year to year, from 34.8 to a record 35.83 (Anderson et al., 2004; Skogseth, Fer, & Haugan, 2005).

Storfjorden is a large (∼190 km long) and deep (∼190 m) bay of the Svalbard Archipelago, bordered by the islands of Spitsbergen, Barentsøya and Edgeøya and marked at its mouth to the Barents Sea by a 120-m deep sill at 77°N (Figure 1). South of the fjord, Storfjordrenna, a trough bordered by the shallow banks of Storfjordbanken, Hopenbanken and Svalbardbanken (also known as Spitsbergen Bank) offers a natural conduit down to the continental slope of western Svalbard.

Storfjorden hosts a recurrent latent heat polynya in winter where considerable volumes of ice, of order 30–50 km^3, are formed annually, releasing about 1 gigaton of salt in the ocean, which is known to be the primary source of the local BSW formation (Haarpaintner, 1999; Haarpaintner, Gascard, & Haugan, 2001; Iwamoto et al., 2014; Jardon et al., 2014; Preußer et al., 2015; Rousset et al., 2015; Skogseth et al., 2004, 2008). The seasonal cycle of dense water production and overflow in Storfjorden was summarized by Skogseth, Fer, and Haugan (2005) as follows. In the early freezing period the dense water produced by brine release gradually fills the depressions of the fjord, reaching the sill level and generating a weak overflow. The latter strengthens and reaches a steady state between March and May, fueled by the transformation of inflow waters into BSW. Depending on brine production, more

than the entire volume of Storfjorden can be flushed by this process during the freezing period (Skogseth, Haugan, & Jakobsson, 2005; Skogseth et al., 2008). The overflow continues in summer, but gradually weakens. Toward October, dense water is trapped behind the sill with occasional discharge triggered by atmospheric forcing. When averaged over 1 year, this intermittent cycle produces a typical flow of 0.03–0.04 Sv (1 Sv $\equiv 10^6$ m^3 s^{-1}) of BSW according to a polynya model (Skogseth, Fer, & Haugan, 2005; Skogseth et al., 2004). This is slightly lower, but generally consistent with, the previous estimate of 0.05 Sv by Schauer (1995), since the latter was based on measurements 30 km downstream of the sill and thus includes a contribution of entrained ambient water. This cycle was further confirmed from 4 years of current meter observations at the sill by Geyer et al. (2009) who found that the overflow starts between late January and mid March, and stops no earlier than mid August and up to late September, with an annual average transport of 0.03 Sv. Overflowing BSW continues as a plume of dense water along the northern slope of Storfjordrenna (e.g., Fer et al., 2003; Schauer, 1995).

While the annual BSW volume transport appears relatively constant (e.g., Geyer et al., 2009), the density of the overflow, which determines its subsequent insertion into the deep ocean, varies widely on interannual time scales following the salinity of the BSW formed in the polynya. The latter fluctuates under the influence of several factors. These factors include: the volume of ice forming over the winter season (Jardon et al., 2014; Schauer, 1995; Skogseth et al., 2004), which is primarily driven by atmospheric conditions; and the location of the polynya with respect to the bathymetry, that is, whether the rejected brine is diluted into a thin or thick water column (Haarpaintner, Gascard, & Haugan, 2001). Another influential factor is the preconditioning, that is, the initial salinity of the source water being transformed (Schauer, 1995; Skogseth et al., 2004). BSW forms primarily from Arctic Water (ArW), the salinity of which varies in the northwestern Barents Sea with the volume of ice exported from the Arctic Ocean and melting there (Maus, 2003). Skogseth, Haugan, and Jakobsson (2005) further pointed out that particularly saline BSW may result from intrusion of an underlying water layer of Atlantic origin. The Polar Front (PF), which marks the boundary between water originating from the Arctic and water of subtropical origin coming from the North Atlantic, is located close to the mouth of Storfjorden. In the Barents Sea the PF is reported to be locked to the bathymetry, approximately following the 150 m isobath in summer (Loeng, 1991) or the 220 m isobath according to Barton et al. (2018). The PF, therefore, follows a winding pathway in the region: North Atlantic Water (NAW) engulfs Storfjordrenna carried by a branch of the Norwegian Atlantic Current (NAC) that is topographically guided and flows cyclonically (Figure 1, right). Given its potential impact on the characteristics of the locally formed dense water, it is important to document the summer hydrography of Storfjorden.

In this paper we present an analysis of water masses and evaluate the transport of the different currents of the Storfjorden-Storfjordrenna system from a comprehensive set of hydrographic observations collected in July 2016 during the *STEP* (Storfjorden Polynya multidisciplinary study) cruise onboard R/V *L'Atalante*. Besides providing a synoptic view of water masses and currents, the analyses will focus on the BSW produced during the preceding winter, from Storfjorden, where remnants are expected to be stored, to Storfjordrenna where it is expected to overflow as a dense plume. We will compare in particular our results with the comprehensive picture of water mass transformation in Storfjorden provided by Skogseth, Haugan, and Jakobsson (2005) based on data collected between 1999 and 2002.

The paper is organized as follows. The data set and processing methods are described in Section 2. In Section 3, we first present in some detail the hydrographic characteristics of the region, distinguishing the inner fjord area from the regions south of the sill, before synthesizing the horizontal circulation. Section 3 is concluded by an analysis of the essentially three-dimensional circulation in Storfjorden in an isopycnal framework, with a focus on water mass transformation. These results are discussed and contrasted to the existing literature in Section 4, considering in particular the specificities of the year 2016 in terms of atmospheric forcing. The main findings are summarized in Section 5.

2. Data and Methods

A network of 46 hydrographic stations was occupied on different sections across Storfjorden and Storfjordrenna between 12 and 19 July 2016 (Figure 1) as part of the STEP 2016 cruise (Michel & Vivier, 2016). All hydrographic profiles were collected with a Seabird SBE911plus conductivity-temperature-depth (CTD) probe with an accuracy of ±0.001°C for temperature and ±0.003 mS/cm for conductivity. The accuracy of salinity measurements was assessed with a Guildline's Autosal laboratory salinometer (OSIL) from 33 water samples collected at various

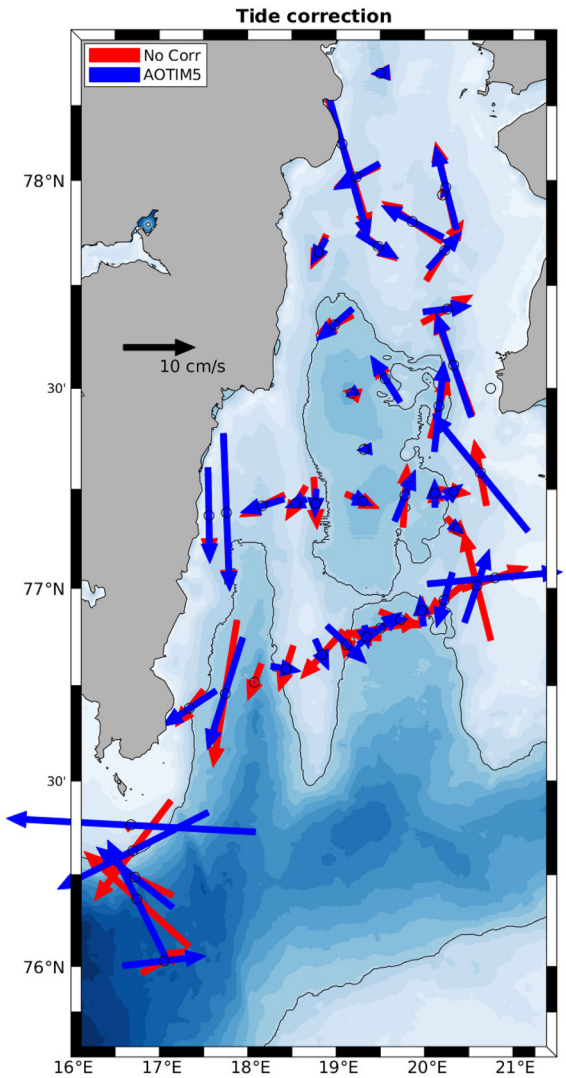

Figure 2. Map of the depth-averaged velocity from the lowered-acoustic Doppler current profiler uncorrected from tides (red) as well as detided with the AOTIM5 tide model (blue). Bathymetry is from Smith and Sandwell (1997, v19.1).

depths ranging from 5 to 350 m between Stations 2 and 46. The salinity bias (Autosal −CTD) was −0.0015 with a root mean squared error of 0.0009, well within the precision range of CTD sensors; a post cruise correction of CTD data was therefore not deemed necessary. Dissolved oxygen concentration was measured with a Seabird SBE43 sensor attached to the rosette. Oxygen data were calibrated with ex-situ titrations (Winkler method, Grasshoff et al., 1983) from water samples taken at eight stations (three depths per station) regularly spaced during the cruise, which demonstrated an agreement to within less than 2 μmol kg^{-1} with no detectable drift during the cruise. In subsequent analyses hydrographic data have been processed with the Gibbs Sea Water toolbox implementing the Thermodynamic Equations of Sea Water 2010 (TEOS-10) (McDougall & Barker, 2011), for example, to compute dynamic height anomaly and geostrophic velocity. However, we shall present practical salinity and potential temperature rather than absolute salinity and conservative temperature for the sake of comparison with the abundant existing literature.

Velocity profiles were collected at each station from a lowered-acoustic Doppler current profiler (LADCP) composed of an up-looking and a down-looking 300 kHz Workhorse Sentinel ADCP from Teledyne RD Instruments. Velocity profiles were also collected underway using a vessel-mounted ADCP operating at 150 kHz (Teledyne RD Instruments' Ocean Surveyor). LADCP data were processed based on the velocity inversion method developed a the Lamont-Doherty Earth Observatory (LDEO software version 9, Thurnherr, 2014) and shipborne ADCP (SADCP) data were processed with CASCADE version 7 (Le Bot et al., 2011). The residual error depends on the station and ranges between 3 and 6 cm s^{-1} for most stations; however, errors exceed 10 cm s^{-1} at a few stations (36–38, 41–43), and the data therefore need to be considered with caution.

ADCP data are impacted by tidal currents. These were estimated using the Tide Model Driver (TMD v2.5) package developed by Earth and Space Research, using three different tide models: the Arctic Ocean 5 km Inverse Model 2018 (Arc5km2018) and the Arctic Ocean 5 km Inverse Model (AOTIM5; Padman & Erofeeva, 2004) as well as TPXO9v4 (Egbert & Erofeeva, 2002). Tidal currents are generally small (<5 cm s^{-1} in amplitude) except near Sørkapp (Station 42) and to a lesser extent on Storfjordbanken south of Edgeøya (Stations 27, 29, and 30), with sometimes large discrepancies between models, which makes a systematic correction somewhat hazardous (Figure 2). The orientation of the depth-average current is, however, better aligned with topographic contours near Sørkapp when detided with AOTIM5, which was therefore used hereafter.

We computed the geostrophic velocity profile between two stations with a reference level set at 40 dbar and shifted with the across-section component of the SADCP velocity field at this specific depth and position. We used the median of the SADCP velocity field while in transit between the two stations as the mid-station velocity profile. We chose a reference depth of 40 dbar as a trade-off to be shallower than the shallowest stations while deep enough so as to minimize the influence of Ekman currents. In the absence of SADCP data (i.e., for sections composed of non-sequential stations), the geostrophic velocity profiles are derived assuming the bottom velocity to be zero. A separate estimate of the cross-section velocity was obtained from the appropriate projection of in-station LADCP data.

Below, we discuss a series of vertical (depth-distance) sections which involved the mapping of hydrographic or velocity profiles at successive stations. Velocity sections were mapped using an objective analysis based on a Gaussian correlation function with a vertical and horizontal length scales of 10 m and 20 km, respectively. The vertical scale was determined from the auto-correlation function of the data whereas the horizontal scale was

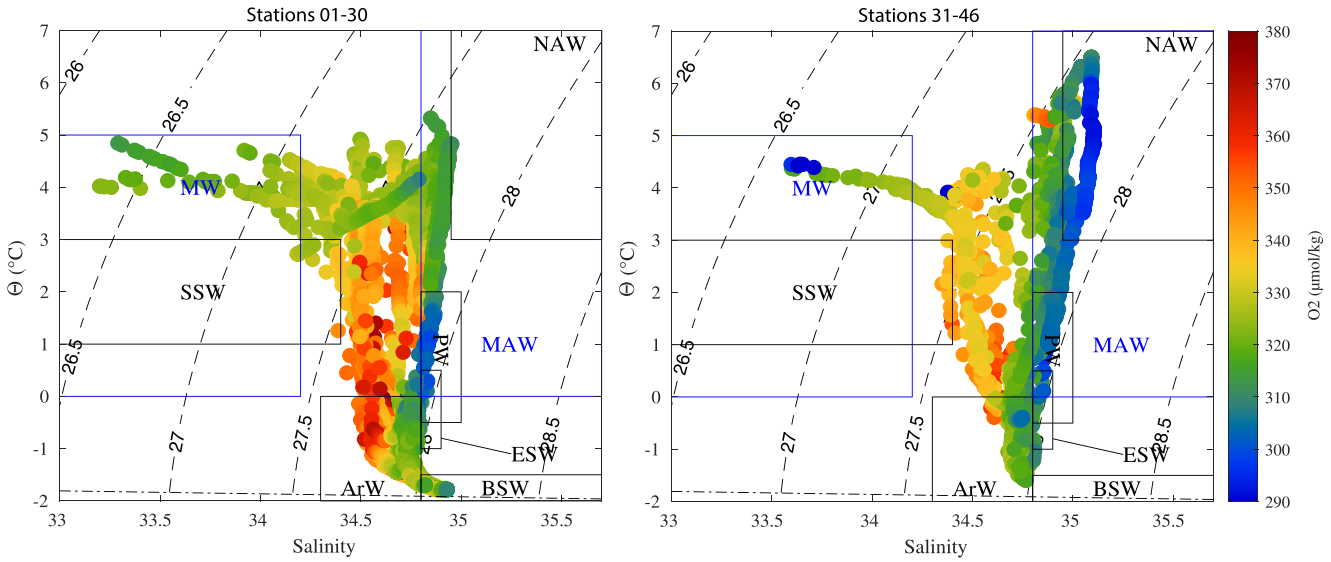

Figure 3. Potential temperature—salinity diagrams for all stations north (left) and south (right) of the Storfjorden sill at 77°N. The color denotes the dissolved oxygen concentration (in μmol kg^{-1}). See Table 1 for the acronym of water masses.

set from practical considerations (inter-station distance). The horizontal and vertical resolutions of interpolated fields are 1 km and 1 m, respectively. Unless otherwise noted, mapped velocity fields merge the mid-station SADCP-shifted geostrophic velocity profiles and in-station LADCP profiles for an increased spatial resolution. A cumulative volume transport was estimated by summing over depth from the specified boundaries of the section. Likewise, gridded velocity fields were used to estimate the volume transport on a given density range. The mapping of hydrographic data was obtained by fitting a surface using a modified ridge estimator (Hoerl & Kennard, 1970) with a gradient regularization (D'Errico, 2006). The grid was first non-dimensionalized using the same vertical and horizontal scales as above. This approach was preferred to objective analysis as it allowed a better tuning of the smoothness of the mapped field so as to limit, as much as possible, the generation of unphysical values between profiles (e.g., spurious temperatures below the freezing point).

Ancillary data for this study include the merged infrared-microwave Sea Surface Temperature (SST) product from Remote Sensing Systems (http://www.remss.com), wind stress and air temperature, taken from the European Centre for Medium-Range Weather Forecasts (ECMWF) Reanalysis (ERA)-Interim (Dee et al., 2011), and sea ice concentration from the Advanced Microwave Scanning Radiometer (AMSRE and AMSR2) satellite data (Spreen et al., 2008).

3. Results

A satellite SST image concurrent with the cruise (Figure 1, right) shows that the upper ocean hydrography in Storfjordrenna is dominated by Atlantic Water (AW) whilst water of Arctic origin predominates in Storfjorden. To distinguish hydrographic characteristics of the inner fjord to the north from that to the south of the sill, we set a boundary at 77°N. As we shall show below, this boundary at the latitude of the sill is merely schematic and is permeable to water of different origins.

3.1. Inner Fjord

The potential temperature-salinity (Θ–S) diagram of all stations north of the sill is shown in Figure 3 (left). In the diagram, water masses are labeled according to the classification compiled by Skogseth, Haugan, and Jakobsson (2005) and reproduced in Table 1, distinguishing waters of predominately Atlantic and Arctic origins. ArW is found at nearly all stations except for those to the southeast of Storfjorden. As will be confirmed by depth-distance sections, Melt Water (MW) is not very abundant, nor is Storfjorden Surface Water (SSW) that is a product of the mixing of ArW and MW generally found in the upper 60 m (Haarpaintner, O'Dwyer, et al., 2001).

Table 1
Watermasses in Storfjorden and Storfjordrenna (From Skogseth, Haugan, and Jakobsson (2005))

Arctic only			
Arctic Water	ArW	$\theta \leq 0.0°C$	$34.3 \leq S \leq 34.8$
Brine-enriched Shelf Water	BSW	$\theta < -1.5°C$	$S > 34.8$
Melt Water	MW	$\theta > 0.0°C$	$S < 34.2$
Storfjorden Surface Water	SSW	$1 \leq \theta \leq 3.0°C$	$S < 34.4$
Atlantic Water and mixtures			
North Atlantic Water	NAW	$\theta > 3.0°C$	$S > 35$
Modified Atlantic Water[a]	MAW	$\theta > 0.0°C$	$S > 34.8$
Polar Front Water[a]	PW	$-0.5 \leq \theta \leq 2.0°C$	$34.8 \leq S \leq 35$
East Spitsbergen Water[a]	ESW	$-1 \leq \theta \leq 0.5°C$	$34.8 \leq S \leq 34.9$

[a]MAW, PW and ESW are all formed through mixing between NAW and ArW along the Polar Front, but in different geographic locations.

We identify the dense BSW locally formed in Storfjorden during the winter and remaining in the depressions in summer, as described by different authors (e.g., Quadfasel et al., 1988; Schauer, 1995). The densest BSW, sampled at Station 23, has a salinity of 34.95 and a potential density anomaly $\sigma_\theta = 28.12$ kg m^{-3}, which places it on the fresh and light side of BSW. The latter experiences substantial interannual variability with a maximum salinity ranging between 34.8 and 35.8 (Skogseth, Fer, & Haugan, 2005).

Pure NAW is absent north of the sill; however, we do find water of Atlantic origin primarily to the southeast of the fjord. These include Polar Front Water (PW) that is formed by the mixing of Arctic with AW at the PF in the Barents Sea (Haarpaintner, O'Dwyer, et al., 2001; Loeng, 1991) and, more broadly, Modified Atlantic Water (MAW) that flows along the PF south of Storfjorden (Schauer, 1995). East Spitsbergen Water (ESW), which is transported with the eponymous current and was originally identified by Quadfasel et al. (1988) west of Hopenbanken, is only marginally found to the southeast of the fjord; its identification is ambiguous here as hydrographic characteristics are also consistent with that of PW. MAW, ESW, and PW are all formed by the mixing of Atlantic and ArW but at different geographic locations along the PF.

The dissolved O_2 concentrations range between 300 μmol kg^{-1} for PW or the deepest BSW and 380 μmol kg^{-1} for ArW. We note, however, that oxygen is not a distinct tracer of individual water masses (e.g., ArW spans a wide range of values), but seems primarily to correlate with depth. In general, deeper layers are more depleted in oxygen. However, the shallowest layer (water lighter than ~27.5 kg m^{-3}; Figure 3, left) also shows low oxygen levels, assumed to be caused by enhanced biological activity. The distribution of oxygen data in the $\theta - S$ space suggests significant mixing of ArW with less oxygenated AW, as will appear more distinctly in an isopycnal framework (Section 3.4).

The spatial distribution of the different water masses inside Storfjorden is depicted by the zonal and meridional sections shown in Figures 4 and 5, respectively. The zonal section at 77°15' N shows fresh MW at the surface most clearly to the west, narrowly channeled by the cyclonic Coastal Current (CC). There is further MW present to the east, suggesting that it is brought about from the Arctic by the East Spitsbergen Current (ESC), with possible freshwater addition from runoff inside Storfjorden. The MW is consistently present at Stations 7–11 (Figure 1) to the northeast of Storfjorden (not shown) and otherwise absent in the fjord interior (Figure 5).

BSW is found in the deepest depression, from the bottom up to a depth of 90 m, which is above the sill level (120 m). Remnant BSW is also found at the bottom of a shallower depression at the northernmost Station 2 (Figure 5). Above the BSW layer, ArW occupies the largest volume of water in Storfjorden, apparent as a subsurface layer between 120 and 50 m (Figure 4), rising up to 20 m at the center of the deepest depression (Station 17) as shown in Figure 5. The latter section nearly repeats the meridional CTD transect along 19°E occupied in July 1999 and discussed by Haarpaintner, O'Dwyer, et al. (2001, their Figure 4). These authors separated summer stratification in Storfjorden into three layers: the dense BSW layer, an Arctic intermediate layer and the SSW layer in the upper 60 m. By contrast, we find very little SSW. SSW is a mixture of ArW and meltwater, heated by the atmosphere to a characteristic temperature of 1–3°C and with a salinity lower than 34.4 (Haarpaintner,

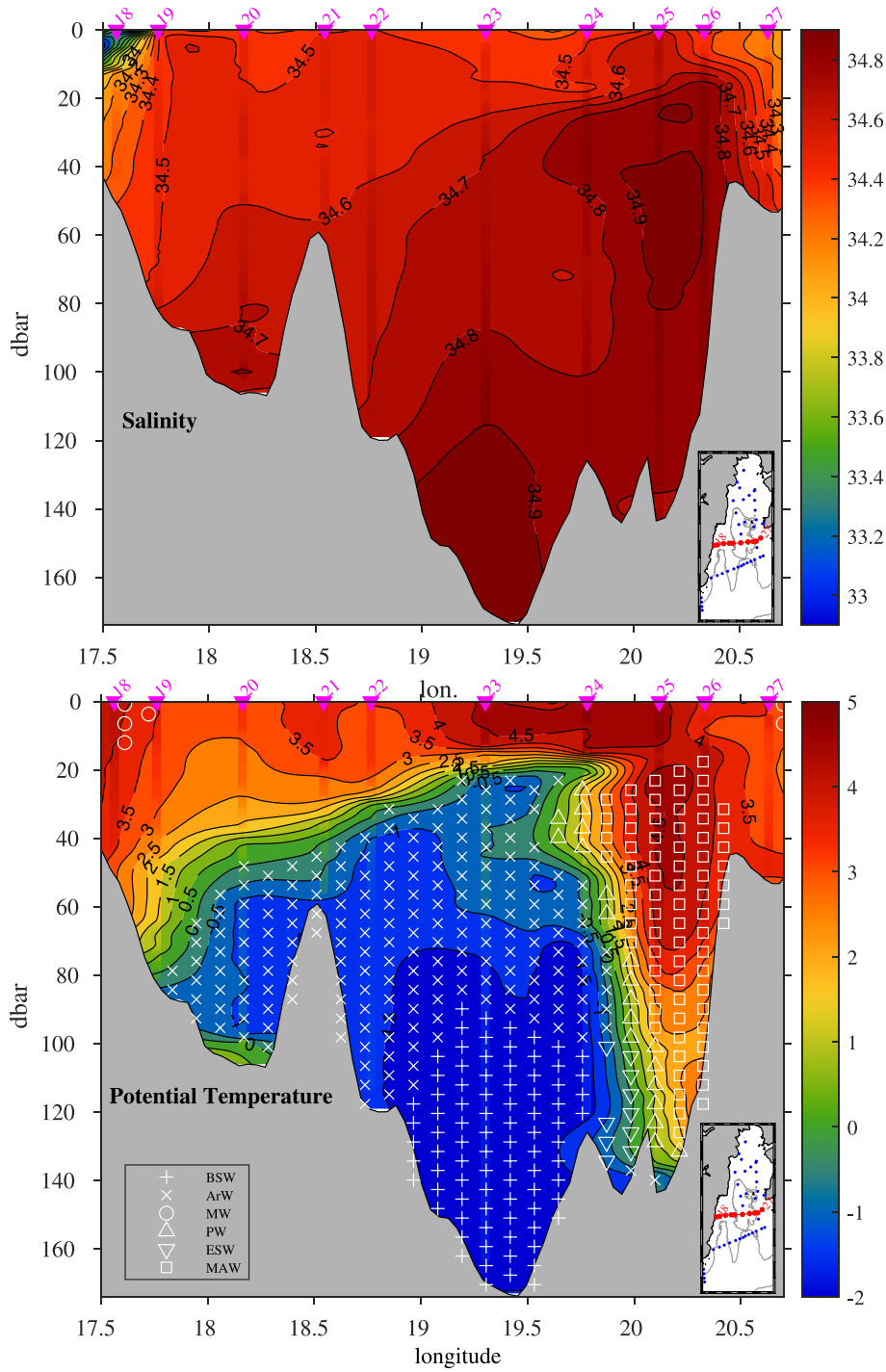

Figure 4. Salinity (top) and potential temperature (bottom) distribution on the zonal section at 77°15'N (temperature units in °C).

O'Dwyer, et al., 2001). Here the bulk of the water in the upper 50 m of the section has a salinity greater than 34.4, suggesting that it is merely ArW that has warmed without mixing with fresh MW, the latter being only present to the periphery of Storfjorden conveyed by the CC. We note, however, that water with the characteristics of SSW is brought by the ESC at Station 27.

MAW enters the fjord to the east between a depth of 20 m and the bottom at 130 m. It is bordered to the west by PW that marks the boundary with the superimposed layers of ArW and BSW underneath (Figure 4). MAW and

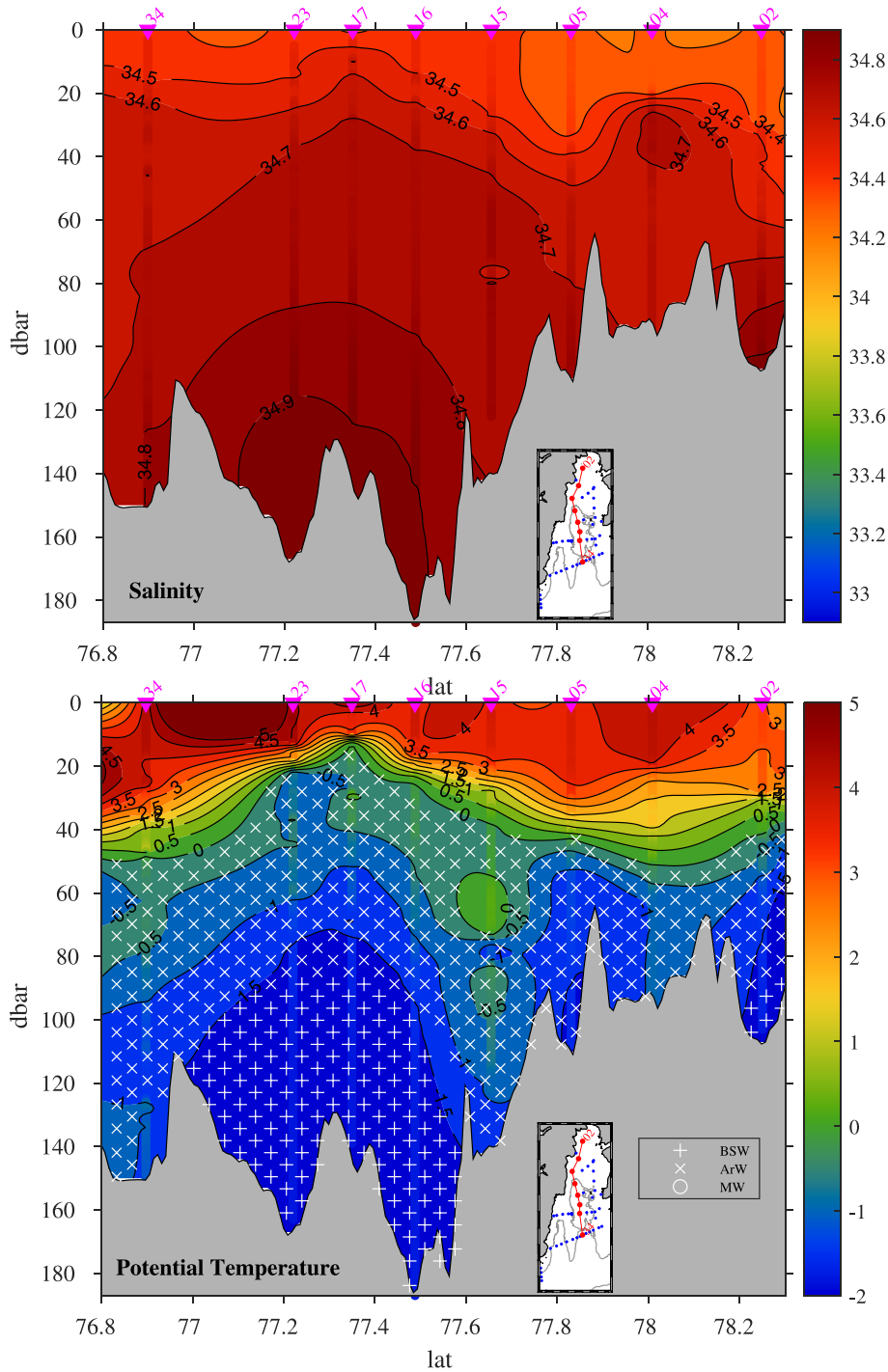

Figure 5. Salinity (top) and potential temperature (bottom) fields on the meridional section in the middle of Storfjorden (temperature units in °C).

PW flow northward above 100 m depth with a velocity on the order of 10–15 cm s^{-1} (Figure 6a). These water masses are absent from the meridional section of Figure 5, which is positioned too far to the west but they can be tracked at the different stations along 20°E up to Station 13 throughout the water column, extending further north as a 20 m-thick bottom layer up to Station 10 at 77°40'N as we shall see later (Section 3.3). This is quite a long way inside Storfjorden in the area where the polynya is most active in winter, west of Edgeøya (Skogseth, Fer, & Haugan, 2005; Skogseth et al., 2004).

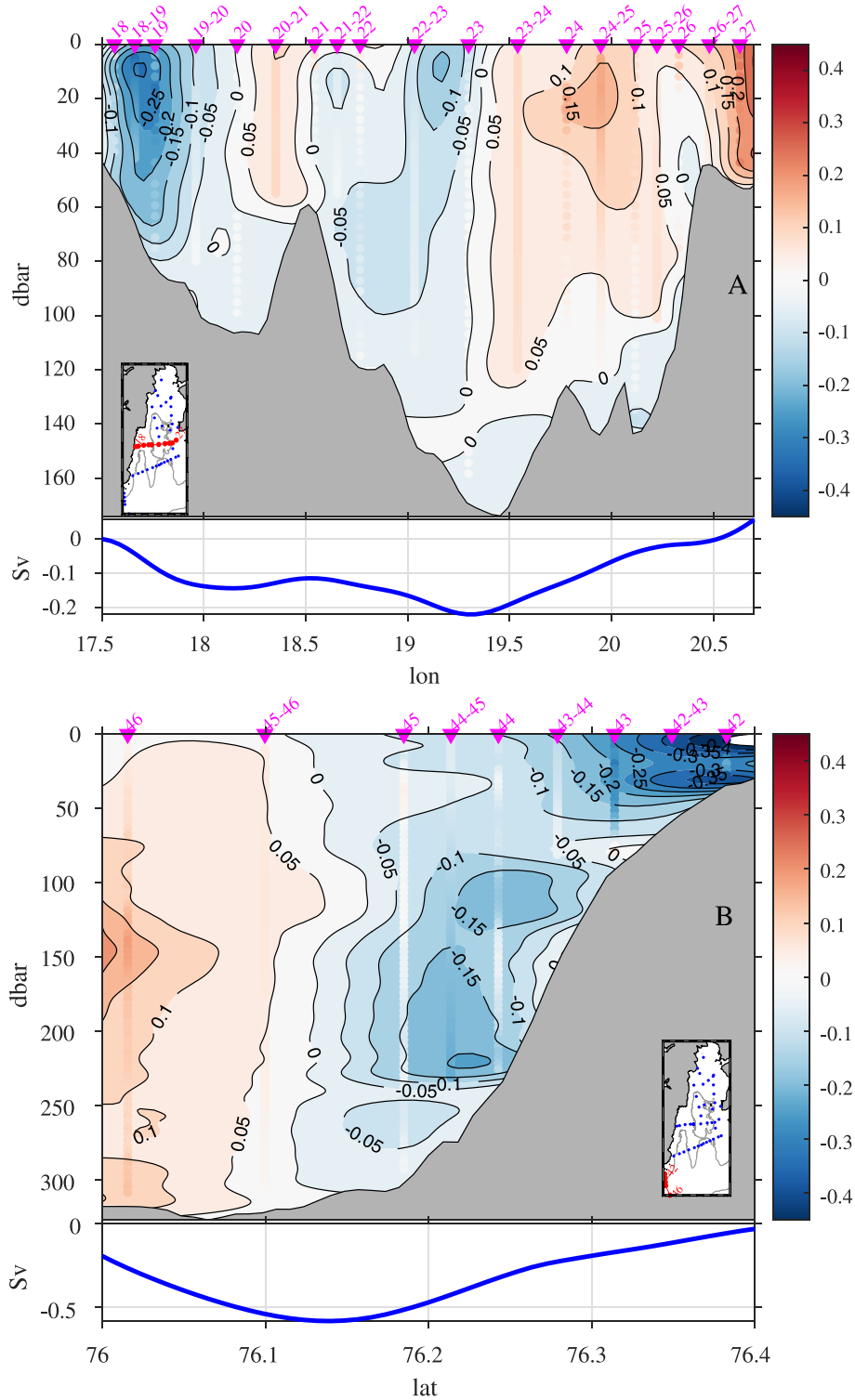

Figure 6. Velocity field perpendicular to the zonal section at 77°15'N (a) and to the meridional section south of Sørkapp (b). Velocity fields are obtained from the merge of hydrographic, shipborne acoustic Doppler current profiler and lowered-acoustic Doppler current profiler data. Positive values are northward and eastward, respectively (units in m s^{-1}). The subplot at the bottom of each velocity section denotes the corresponding cumulative volume transport from the western (northern) boundary (units in Sv).

The velocity section at 77°15'N (Figure 6a) clearly features the cyclonic CC conveying MW in the upper 15 m. The CC is entirely captured to the west but only partially sampled to the east. To the west, the southward branch is located between the 40 and 90 m isobaths with core velocities exceeding 25 cm s^{-1} above the 70 m isobath. It reaches down to 80 m. The transport associated with the CC is 0.14 Sv (Figure 6a, bottom) which exceeds the four estimates reported by Skogseth, Haugan, and Jakobsson (2005), which range from 0.04 Sv for three cruises in the summer/fall 1999, 2000, and 2002, to 0.11 Sv for a cruise in August 2001 that stands out as a peculiar year. We note that these estimates are for the baroclinic component only, so that our estimate, which is to our knowledge the first direct estimate, is consistent with that reported for August 2001. Only two thirds of the transport of the CC inflow is captured to the east (assuming volume transport conservation between the entering and exiting branch), the remainder flowing as a wider current on the shallow Storfjordbanken which was not occupied by the section.

The velocity section also features a cyclonic circulation centered on the main depression with an associated balanced transport on the order of 0.10–0.15 Sv. This cyclonic, topographically guided flow in summer, with inflow on the eastern side associated with warmer and more saline water to the east has been reported earlier (Fer et al., 2003; Schauer, 1995; Skogseth, Haugan, & Jakobsson, 2005), albeit just south of the sill. The northward inflow of MAW is 0.06 Sv which amounts to 0.08 Sv including PW. A secondary weak cyclonic circulation is apparent to the west of the meridional ridge. The 0.05 Sv transport imbalance to the east of the section (Figure 6a, bottom) indicates a cumulative error on the transport on the order of 0.1 Sv since about a third of the CC inflow is missing from the section to the east (neglecting in this calculation a possible contribution from the northwestern Barents Sea through the two sounds to the north of Storfjorden, Freemansundet and Heleysundet).

3.2. South of the Sill

3.2.1. Water Masses and Circulation

The Θ–S plot of Figure 3 (right) reveals that water of Atlantic origin, including saltier and warmer pure NAW characterized by low oxygen values (minimum 291 μmol kg^{-1}), are quite ubiquitous. On the contrary, dense BSW is absent south of the sill. However, a few points with a salinity slightly larger than 34.8 and a temperature comprised between −1.5°C and −1°C, that is colder than ESW, are apparent suggesting diapycnal mixing of BSW with warmer ambient water either ArW, PW, or ESW.

The zonal section south of the sill (Figure 7) presents a distribution of water masses that bears some similarities with its counterpart north of the sill (Figure 4) except for the absence of dense BSW. It features a shallow layer of MW entering the fjord to the east and exiting to the west with the cyclonic CC, and a layer of ArW flowing out the fjord bounded to its east by an interleaved branch of Atlantic waters entering the fjord. A striking difference with Figure 4, however, is that this pattern is repeated on both sides of the meridional ridge west of the sill, indicating a meandering of the PF with this topographic structure, as suggested by the SST image of Figure 1 (right). South of the sill, we note the presence of a deep layer of ESW to the east of Station 34, fresher and colder than the PW layer above. A patch of ESW is also found at Station 35 at a depth of 100 m.

The meridional section across Storfjordrenna slope south of Sørkapp (Figure 8) predominantly features water of Atlantic origin; however, there is a substantial difference between the southern part of the section displaying the inflow of pure NAW into Storfjordrenna throughout the entire water column and the northern slope of Storfjordrenna where the outflowing Atlantic waters present the more complex interleaving structure described previously. There, the pure NAW is wrapped in an envelope of MAW, which is bordered by a branch of PW at depth greater than 150 m. Intertwined in Atlantic waters, two branches (or lenses) of cold and less saline water of Arctic origin are apparent at a depth of 75 and 175 m, respectively, associated with a high oxygen content (>325 μmol kg^{-1}; not shown) well contrasted with that of AW. Their respective width cannot be determined accurately as it is sensitive to the scale of the interpolation scheme, but it does not exceed 20 km. We note that an eddy-type circulation in Storfjordrenna with cold lenses was previously reported by Piechura (1996). An alternative hypothesis is that a branch of inflowing NAW at 100 m is retroflected toward the Norwegian/Greenland Seas, bending northward and cutting the outflow of water of Arctic origin.

Finally, the section clearly captures to the north the shallow Sørkapp Current, also known as Spitsbergen Polar Current (Helland-Hansen & Nansen, 1909; Nilsen et al., 2016), confined here over depths shallower than 100 m. This current, which is merely the continuation of the CC sampled in Storfjorden, conveys fresh MW and modified ArW along the west coast of Spitsbergen. It has core velocities exceeding 45 cm s^{-1} (Figure 6b), and is associated with a westward transport of 0.14 Sv (Figure 6b, bottom), consistent with the estimate of the CC in Storfjorden

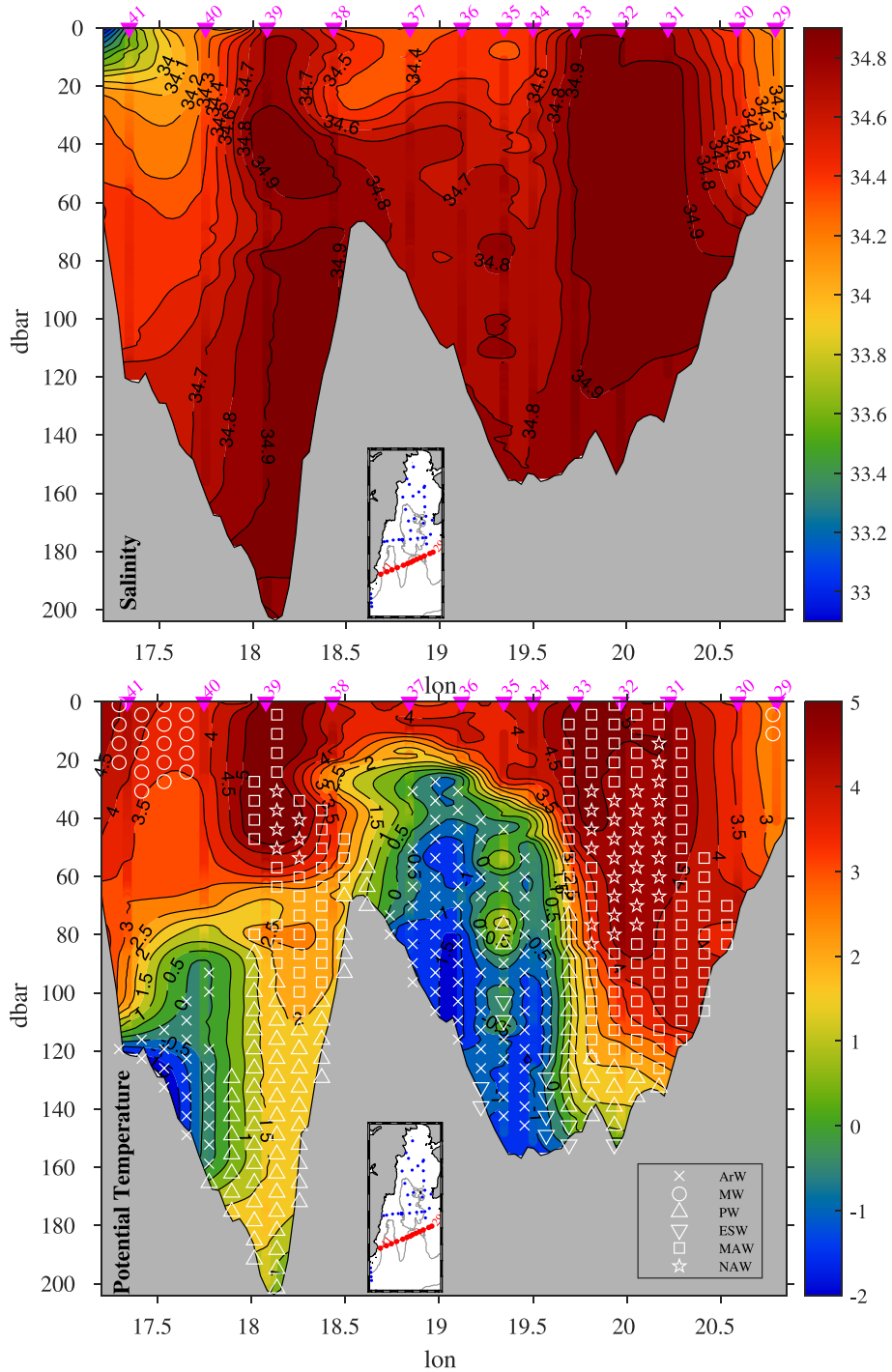

Figure 7. Salinity (top) and potential temperature (bottom) distribution on the zonal section south of the sill at 77°N (temperature units in °C).

of Figure 6a (bottom). The total outflow (including the CC) from Storfjordrenna into the Norwegian/Greenland Sea is 0.6 Sv according to Figure 6b (bottom).

3.2.2. Overflow of Dense Water

Focusing on the outflow of dense water, we have searched for the possible pressence of a dense plume immediately south of the sill that marks the entrance of Storfjorden as well as on the meridional section further downstream at Sørkapp across Storfjordrenna.

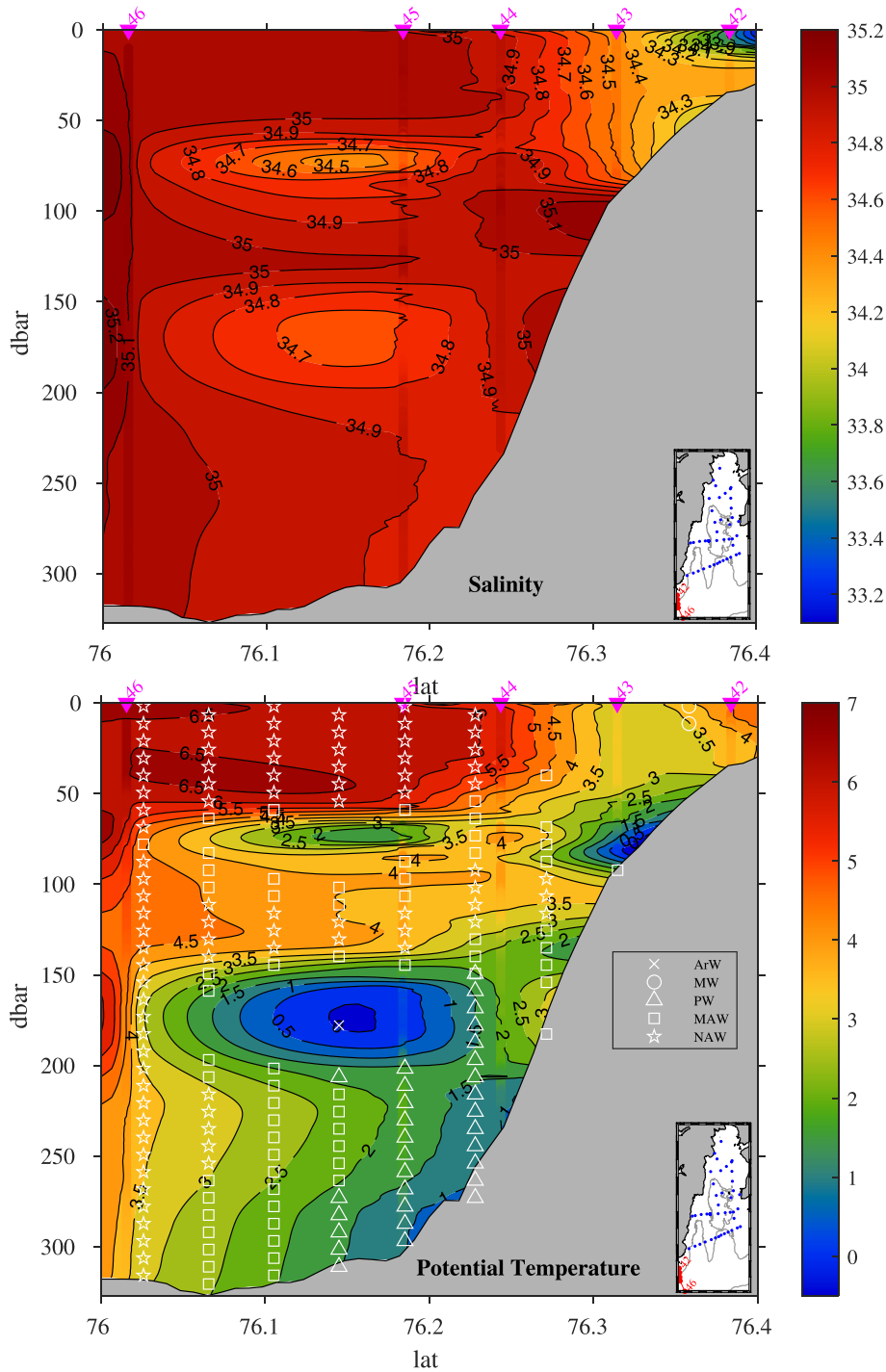

Figure 8. Salinity (top) and potential temperature (bottom) fields on the meridional section south of Sørkapp (temperature units in °C).

South of the sill, there is an indication of a thin bottom layer of saltier water spreading from the bottom of the trough up to the eastern flank of the meridional ridge that borders the sill (Stations 32–36, Figure 7; top). At Station 35 this southward flowing 15-m thick layer has a salinity of 34.80 and a temperature of −1.18°C (Table 2) suggesting mixing of BSW with a fresher and warmer water mass above. The deep layer at Station 34 has quite similar θ–S characteristics but is associated with small northward velocities (Table 2). At Station 36 on the eastern slope of the ridge, over a depth of 122 m (the depth of the sill), the 15-m thick bottom layer is colder and

Table 2
Bottom Layer Properties South of the Sill (Stations 36–32, From West to East) and South of Sørkapp Across Storfjordrenna (Stations 44–45, From North to South)

Station	Depth(m)	Thickness(m)	Θ(°C)	S	σ_θ(kg m^{-3})	u (cm s^{-1})	v (cm s^{-1})	Water mass
36	122	15	−1.59	34.766	27.985	6	**−7**	ArW
35	156	15	−1.18	34.802	28.000	2	**−4**	mix
34	156	23	−1.07	34.802	27.997	4	2	mix
33	151	9	0.47	34.860	27.960	4	**−5**	ESW
32	154	30	0.30–1.90	34.840–34.890	27.890–27.960	−3	**−9**	ESW/PW
44	237	27	1.00–1.40	34.880–34.890	27.940	**−15**	15	PW
45	310	20	1.01–1.03	34.876	27.940	**−5**	6	PW

Note. Zonal (u) and meridional (v) velocities are detided. Bold values denote an effective contribution to the outflow.

fresher, presenting the characteristics of ArW. It is associated with a southward velocity, as is the rest of the layer of ArW above up to a depth of 50 m (not shown), with no indication of a particularly bottom-intensified structure. Toward the eastern part of the sill (Stations 33 and 32) the bottom layer is composed of warmer and saltier ESW that do flow southward. The net transport across the section of water denser than $\sigma_\theta = 28.000$ kg m^{-3} is 0.001 Sv whereas it is 0.002 Sv for water denser than 27.990 kg m^{-3}. Including the ESW and PW that flow southward at the bottom ($-1°C < \theta < 2°C$, $S > 34.8$), the bottom outflow is 0.008 Sv, for a mean density of $\sigma_\theta = 27.940$ kg m^{-3}.

These observations do not support the presence of a gravity driven overflow. Skogseth, Haugan, and Jakobsson (2005) defined an overflow of BSW from the sill to Storfjordrenna as water with $\theta \leq -0.5°C$ and $S \geq 34.9$ ($\sigma_\theta \geq 28.05$ kg m^{-3}) to distinguish from PW and ESW. Here bottom waters south of the sill all have $\sigma_\theta \leq 28.00$ kg m^{-3}. Even with a less stringent criterion on salinity, the weak bottom flow described above bears little resemblance to a gravity driven overflow. Indeed, according to the direct measurements of Geyer et al. (2009) at the sill, the average overflow is characterized by a thickness of 20–50 m with a clearly bottom-enhanced structure, temperatures colder than −1.5°C, median southward velocities of ∼10 cm s^{-1}, and a mean transport during the overflow season of 0.05 Sv.

Regarding the section across Storfjordrenna, there is evidence of a westward 20–30-m thick bottom-attached flow at Stations 44 and 45, apparent as a temperature minimum near the bottom (Figure 8; bottom). The bottom layer has the characteristics of PW with a density of $\sigma_\theta = 27.940$ kg m^{-3} (Table 2). It has the two-layer vertical structure described by Fer et al. (2003) (not shown), but is much warmer and lighter than the plume observed in June 2001 analyzed by these authors ($\sigma_\theta = 28.16$ kg m^{-3}, $\theta = -1.4°C$). The westward volume transport of water denser than $\sigma_\theta = 27.940$ kg m^{-3} is 0.020 Sv. Given its relatively warm temperature, this dense layer is more likely the outflow of the densest class of PW rather than the remnants from a previous overflow.

We note that the densest NAW entering Storfjordrenna at the bottom of Station 46 has a density of $\sigma_\theta = 27.870$ kg m^{-3}, that is lighter than the outflow, so that even in the absence of a BSW overflow, the Storfjorden-Storfjordrenna system remains an area of modification of water masses.

3.3. Synthesis of the Horizontal Circulation

In this section we discuss synoptic views of the distribution and circulation of water masses at a depth of 40 dbar and at the bottom.

We use S and θ fields, along with volume transports between adjacent stations from geostrophic and LADCP velocities, to synthesize the horizontal circulation at 40 dbar in Storfjorden and Storfjordrenna (Figure 9, top). In the figure we distinguish the transport across sections actually occupied by the ship (black arrows) from that across sections, mostly meridional, that are calculated from non-sequential stations (magenta arrows), for which we have assumed a level of no motion at the bottom for the geostrophic velocity in the absence of SADCP data. The depth-averaged velocity at each station from the LADCP is visible in Figure 2. The salinity field is well differentiated between the fjord interior and the coastal band occupied by the fresh CC. By contrast, the most salient

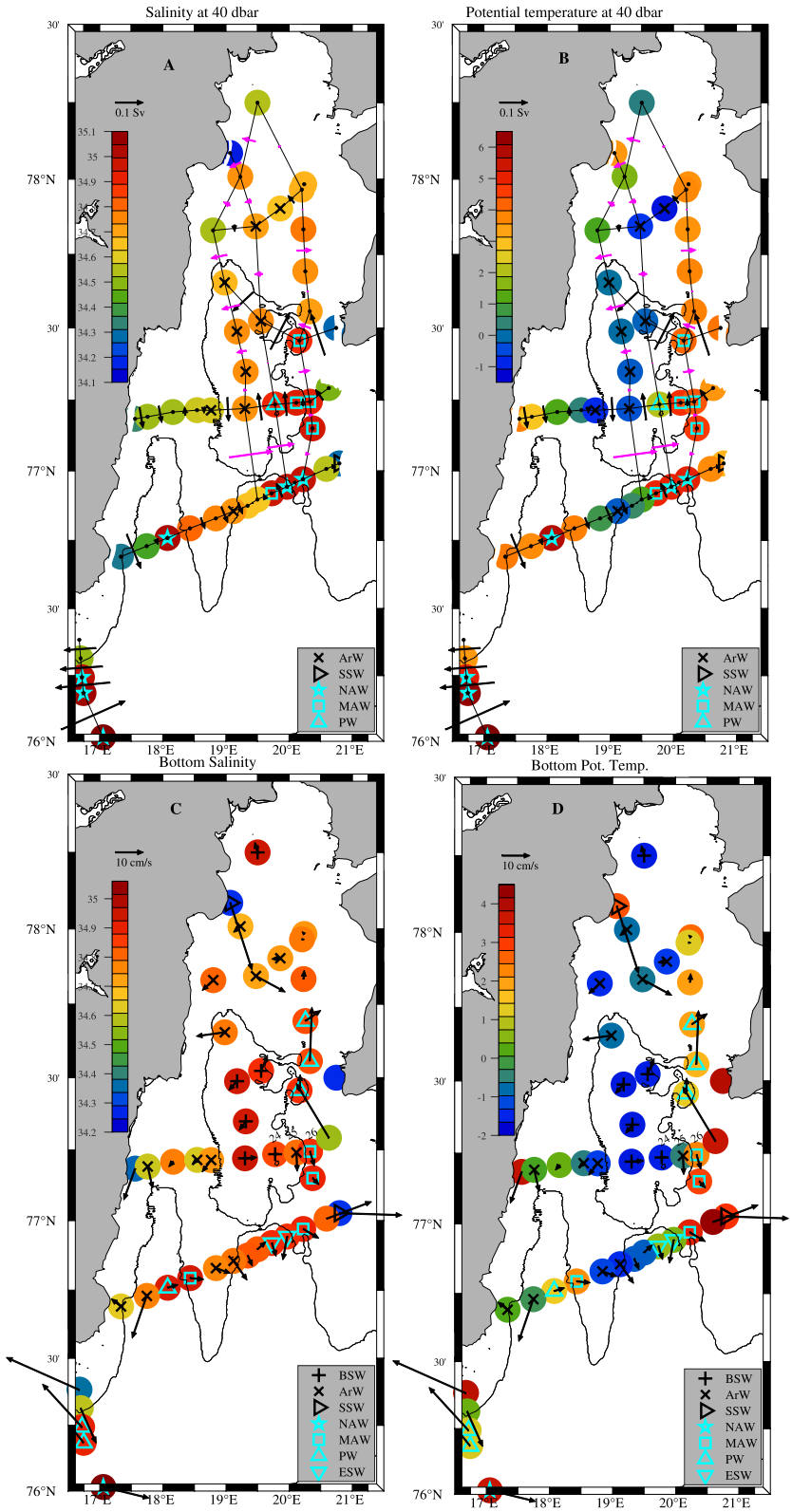

Figure 9.

feature of the temperature field is the marked zonal gradient showing the flooding of water of Atlantic origin to the east of a pool of ArW (Figure 9b). MAW is identified up to 77°30'N at this depth, but anomalously saline and warm water suggestive of admixture of AW is found up to Station 1 at 78°N. Several circulation features discussed previously from distance-depth velocity sections are clearly seen, such as the cyclonic CC, and the cyclonic gyre in the fjord interior (~0.15 Sv) which appears both in the zonal and meridional sections, centered at ~77°15'N and stretched along the meridional direction, following roughly the 120 m isobath. A striking aspect of Figure 9 (top) is the entrapment of ArW in Storfjorden, which flows out with no apparent supply as is visible from the section south of the sill. This is further confirmed by the examination of the corresponding depth-distance velocity section (not shown): the ArW reservoir empties, replaced by the flooding of water of Atlantic origin.

The distribution and circulation of water masses at the bottom (Figure 9, bottom) shows that the shallow periphery of Storfjorden is characterized by the comparatively warmer and fresher cyclonic circulation associated with the CC, with bottom velocities strongly shaped by small scale features of the bathymetry. In the center of the fjord, the cold and salty BSW lines the main depression behind the sill and, as mentioned before, a shallower secondary depression at 78°15'N; BSW is associated with small bottom velocities showing no consistent pattern. The main pool of BSW is bordered by cold ArW to the west and to the north, whereas water of Atlantic origin is found to the east, with a narrow branch of MAW prolonged with PW identified up to 77°40'N. However, as PW spreads northwards, the MAW south of 77°15'N (Station 26) flows to the outside of Storfjorden, as does the ESW at the sill, as previously noted. Since there is no inflow of ESW at other depths, this suggests that ESW was formed locally in Storfjorden rather than brought by the East Spitsbergen Current. On the western half of the sill, we find the outflow of ArW noted previously. Likewise, the bottom plume of PW south of Sørkapp shows up distinctly with a velocity exceeding 20 cm s^{-1}, guided by the bathymetry.

3.4. Isopycnal Framework

As a region of water mass transformation, the circulation in Storfjorden and Storfjordrenna is essentially three-dimensional. The previous horizontal synthesis can only give a rough overview and examining the circulation on isopycnals provides additional insight. Figure 10 displays the potential density anomaly σ_θ across two zonal (left) and two meridional (right) sections in Storfjorden. The isopycnals $\sigma_\theta = 27.87$ kg m^{-3} and $\sigma_\theta = 27.94$ kg m^{-3}, which correspond to the densest NAW inflow and densest PW outflow in/from Storfjordrenna, respectively, at the meridional section south of Sørkapp have been highlighted. The $\sigma_\theta = 27.87$ kg m^{-3} isopycnal raises from a depth of ~300 m at the entrance of Storfjordrenna to the near surface (30 m) in Storfjorden. The overall shape of isopycnals in Storfjorden is that of a dome culminating above the main depression where remnants of the dense BSW ($\sigma_\theta \geq 28.00$ kg m^{-3}) are found, consistent with the cyclonic circulation. The dome shape is, however, strongly asymmetric in the zonal direction with the sharp downward tilting to the east (Figures 10a, 10c) marking the density front associated with the inflow of water of Atlantic origin (PF). PW closely follows the $\sigma_\theta = 27.87$ kg m^{-3} isopycnal in Storfjorden, raising abruptly on top of the ArW layer (Figures 10a, 10d). PW and the densest class of MAW have the same density as the lighter class of ArW, with which they come into contact, conditions favoring isopycnal mixing. A denser class of PW is found at the southern section to the east of the sill and on the western slope of the meridional ridge, limited by the $\sigma_\theta = 27.94$ kg m^{-3} isopycnal (Figure 10c), overlying the ESW layer already discussed. These elements suggest the formation of denser PW and ESW within Storfjorden.

There is direct evidence of water mass transformation in Figure 10 with the presence of unstable density profiles indicating overturns. Focusing on the profiles at stations only to discard spurious instabilities resulting from the mapping procedure, there is indication of overturning to the north of the main depression at Station 15 between 60 and 90 m in the density range comprised between the two highlighted isopycnals (Figure 10b; Figure S1). Likewise, to the northeast of the main depression, an instability is also apparent at Station 14 at approximately the same depth near the $\sigma_\theta = 27.94$ kg m^{-3} isopycnal, with a small inclusion of ESW amid the ArW layer (Figure 10d;

Figure 9. Map of salinity and potential temperature at 40 dbar (top) and at the bottom (bottom) with the volume transport across the different segments between neighboring stations superimposed (top) and the velocity 10 m above the bottom (bottom). The value measured at each station is indicated by color dots whereas the symbol identifies the corresponding water mass. In the top plots the volume transport was estimated from the merge of geostrophic (conductivity-temperature-depth adjusted with shipborne acoustic Doppler current profiler) and detided lowered-acoustic Doppler current profiler velocities. Arrows in black denote the transport for the sections that follow the ship track and for which shipborne acoustic Doppler current profiler data are therefore available to set a reference. The geostrophic velocity for other sections was computed assuming a zero velocity at the bottom; the resulting transport (magenta arrows) is therefore presumed less accurate.

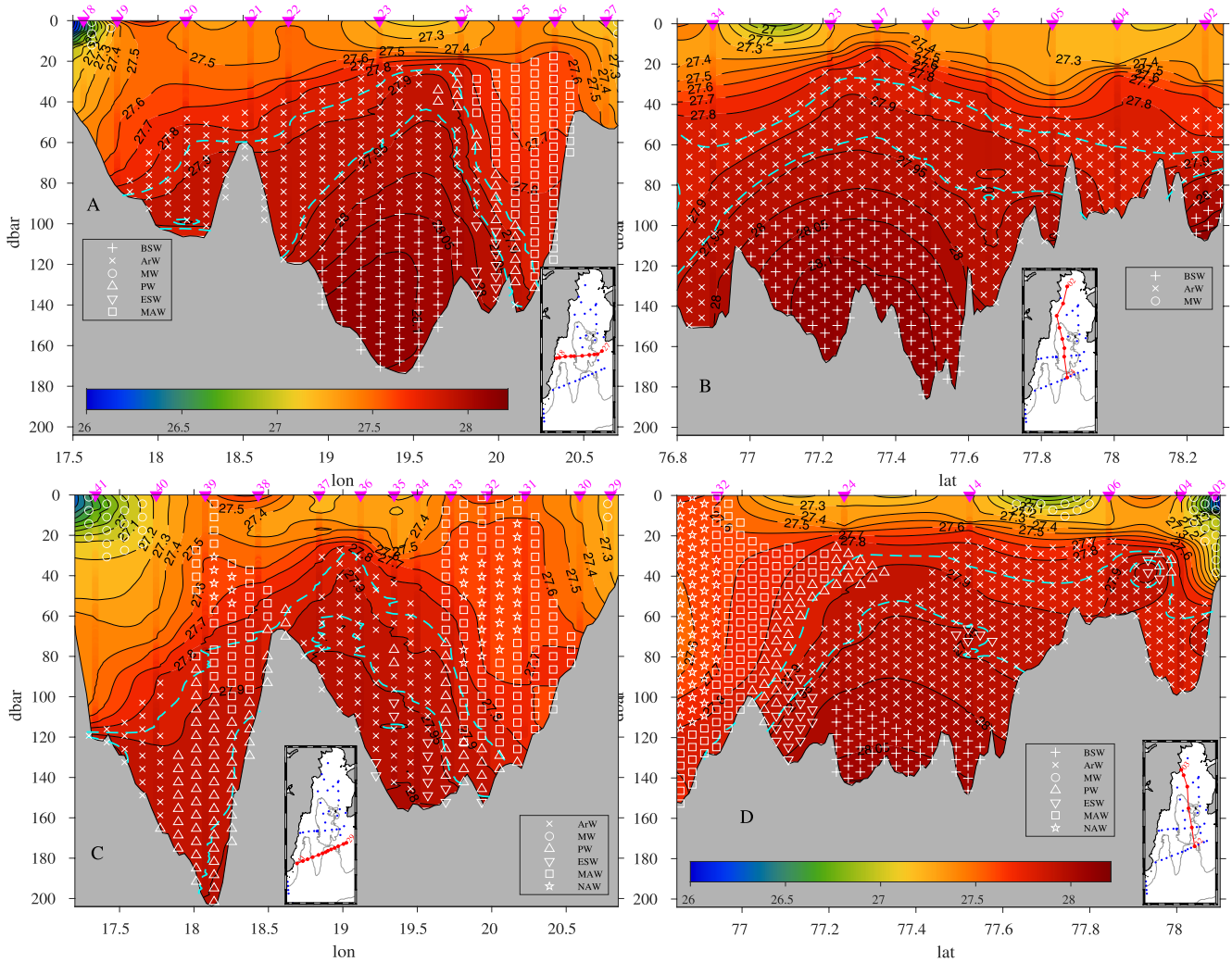

Figure 10. Potential density anomaly σ_θ across two zonal (a and c, left) and two meridional (b and d, right) sections in Storfjorden, with main water masses superimposed. The isopycnals $\sigma_\theta = 27.87$ kg m^{-3} and $\sigma_\theta = 27.94$ kg m^{-3}, which correspond to the densest inflow and densest outflow at the section across Storfjordrenna, respectively, are indicated. Units in kg m^{-3}.

Figure S1). Instabilities are also a quite pervasive feature of the density profiles at the zonal section south of the sill where outflowing ArW comes into contact with water of Atlantic origin on each side of the meridional ridge due to the meandering of the PF (Figure 10c; Figure S1). This is the case for the three stations south of the sill (Stations 35, 36, and 37) between 50 and 110 m (i.e., above the sill level). This area corresponds roughly to the region where Fer et al. (2004) observed the most density overturns in August 2002, which they used to estimate dissipation rate of turbulent kinetic energy and vertical eddy diffusivity. A substantial fraction of their observations of overturns are associated with the dense overflow ($\sigma_\theta > 27.95$ kg m^{-3}) at depths larger than 120 m, which is not the case here. At Station 35, intrusions of PW and ESW are apparent among the ArW layer, distinguishable as well by their lower dissolved oxygen concentration (not shown). On the other side of the meridional ridge, instabilities are also apparent at Station 39 at a depth of 80–90 m where PW and MAW layers are bordered by ArW to the west.

For improved tracking of circulation and transformation of water masses we resort to dissolved oxygen concentration mapped on three isopycnal surfaces (Figure 11): the $\sigma_\theta = 27.80$ kg m^{-3} isopycnal, which marks the top of the ArW layer, the $\sigma_\theta = 27.90$ kg m^{-3} isopycnal, corresponding approximately to that of the densest inflowing NAW, and the $\sigma_\theta = 27.94$ kg m^{-3} isopycnal. The circulation on the $\sigma_\theta = 27.80$ kg m^{-3} isopycnal shows the penetration of the AW branch to the east associated with lower oxygen concentrations, bending westward at 78°N and spreading and mixing southward around the cyclonic gyre in the center of Storfjorden, marked with high oxygen

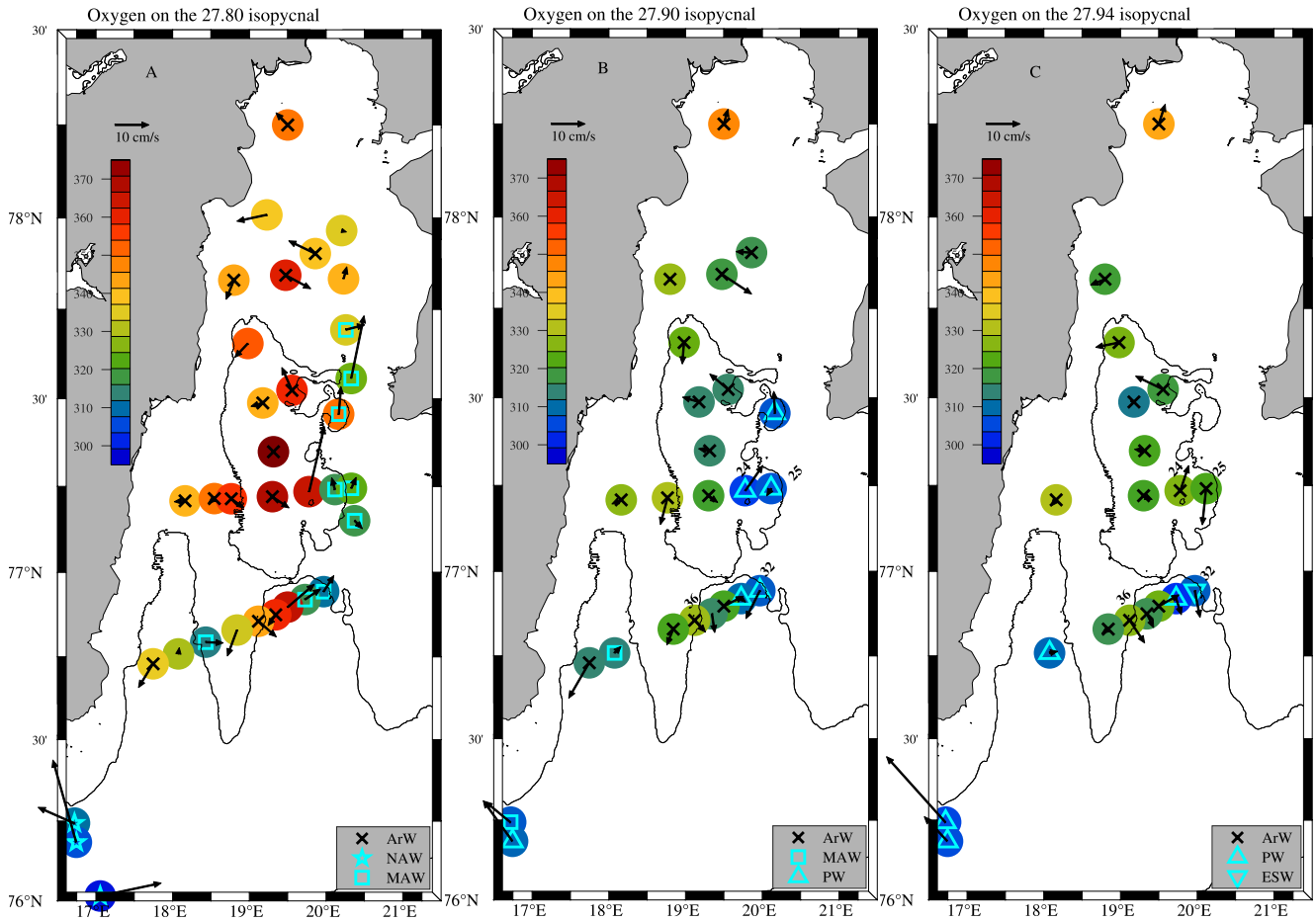

Figure 11. Dissolved oxygen concentration (in μmol kg^{-1}) and velocity (in cm s^{-1}) on the $\sigma_\theta = 27.80$ kg m^{-3} isopycnal (A, left), on the $\sigma_\theta = 27.90$ kg m^{-3} isopycnal (B, middle), and on the $\sigma_\theta = 27.94$ kg m^{-3} isopycnal (C, right). Main water masses are identified by symbols (see Table 1 for acronyms).

concentrations (Figure 11a). The spreading and mixing of the water of Atlantic origin is even clearer on the $\sigma_\theta = 27.90$ kg m^{-3} isopycnal (Figure 11b), with a gradient in oxygen concentration between the southward flowing branch of the gyre to the west and the northward flowing PW with particularly low oxygen content to the east. Part of this inflow retroflects to the east (Station 25) branching to a secondary anticyclonic circulation. Recall that the isopycnal circulation occurs on two very different vertical levels at Stations 24 and 25 with the depth of $\sigma_\theta = 27.90$ kg m^{-3} isopycnal plummeting from 30 to 120 m (Figure 10a). The southward bottom or near-bottom velocity at Stations 25 and 26 was previously pointed out (Figure 9, bottom). The outflow of PW associated with this slanted circulation cell is well visible south of the sill at Station 32 (Figure 11b). This cell of PW overlays a bottom layer of denser ArW with higher oxygen concentration rotating anticyclonically on the $\sigma_\theta = 27.94$ kg m^{-3} isopycnal, constrained by the local topography at Stations 24 and 25 (Figure 11c). The water outflowing at the sill on this same isopycnal at Station 32 has the $\theta - S$ characteristics of ESW as noted before with a slightly higher oxygen content than what it was on the $\sigma_\theta = 27.90$ kg m^{-3} isopycnal, suggesting mixing with the colder and more oxygenated ArW. On the western half of the sill, the outflow is composed of ArW with different oxygen concentrations, marking their history in Storfjorden; that is, whether they originate from the periphery of the cyclonic gyre or whether they experienced enhanced mixing with oxygen depleted AW within the gyre.

The bottom plume in Storfjordrenna south of Sørkapp on the $\sigma_\theta = 27.94$ kg m^{-3} isopycnal has low oxygen concentration (304 µmol kg^{-1}) consistent with that of the ESW and PW exiting at the sill but slightly lower than the denser ArW exiting on the western half of the sill (310–315 µmol kg^{-1}). The latter may, however, contribute to the plume at Sørkapp since its density is larger than 27.98 kg m^{-3} (Table 2) and additional en route mixing with less oxygenated lighter ambient water in Storfjordrenna is likely. The connection between the bottom outflow in Storfjorden and south of Sørkapp can only be hypothesized, however, as dissolved oxygen is not a

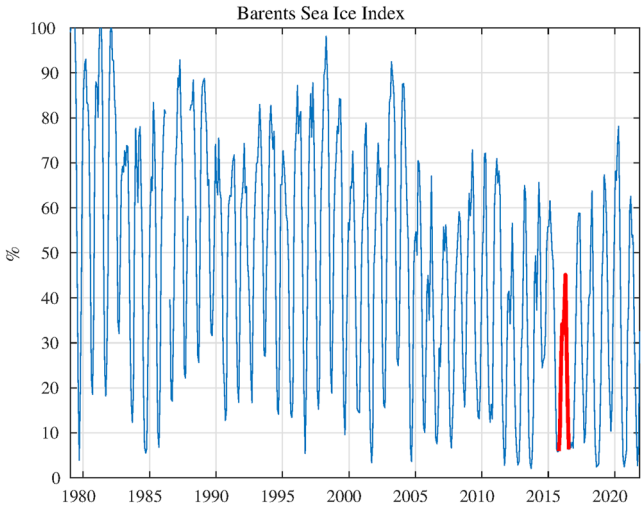

Figure 12. Time series of the Barents Sea Ice Index (in %) provided by EUMETSAT-Ocean and Sea Ice Satellite Application Facilities, defined as the monthly averaged satellite-derived sea-ice extent between 10°E and 60°E and 72°N and 82°N (ice season 2015/2016 in red).

conservative tracer near the bottom due to enhanced biological respiration in the sediments. Furthermore, the flow at the sill requires weeks to months to reach the section at Sørkapp (e.g., Fer & Ådlandsvik, 2008), and conditions in Storfjorden, especially regarding the presence, intensity and properties of a dense overflow at the sill, may have been very different at that time.

4. Discussion

The hydrography and circulation in Storfjorden in the summer 2016 contrasted with those reported previously in several ways. These include the characteristics of the upper water in Storfjorden, which we discuss in relationship with the ice cover during the preceding winter, the absence of an overflow despite a BSW level exceeding the depth of the sill, the flooding of Storfjorden with water of Atlantic origin, and the water mass transformation in these peculiar conditions.

4.1. Surface Hydrography and Winter Ice Cover

As noted in Section 3.1, in the summer 2016 survey there was almost no SSW, which is usually the most pervasive water mass in the upper 60 m of Storfjorden (e.g., Haarpaintner, O'Dwyer, et al., 2001). The SSW was replaced in 2016 by a saltier water mass ($0 < \theta \leq 4.0$°C; $34.4 < S < 34.8$), characterized with a high dissolved oxygen content (~330–350 μmol kg^{-1}), that seems to be ArW that has warmed without mixing with fresh MW. MW was indeed absent over most of Storfjorden except at the periphery where it is brought about by the CC emanating from the ESC. This virtual absence of MW and SSW may be linked to a reduced winter ice cover in the Svalbard region and the northwestern Barents Sea. We have examined the AMRE/AMSR2 satellite sea ice concentration over Storfjorden between 2002 and 2019. On average over 18 years, Storfjorden becomes free of ice as of year-day 175 (23 June). The winter 2015–2016 was marked with particularly mild air temperatures over Svalbard and the northwestern Barents Sea and a reduced ice coverage (not shown). The fjord was free of ice as of 12 May 2016, which is 42 days in advance of the 2002–2019 average date. This early break-up is likely the cause of the small amount of MW encountered in Storfjorden mid-July, and the near absence of SSW that forms from the warming of the fresh surface layer with solar radiation.

Broadening the geographical scope, the winter 2015–2016 standed out as a strongly anomalous year in terms of ice coverage for the entire Barents Sea, amid profound changes at longer time scales. Figure 12 displays the Barents Sea Ice Index (BSII) provided by the EUMETSAT Ocean and Sea Ice Satellite Application Facilities, defined as the monthly averaged sea-ice extent over the Barents Sea (10°–60°E; 72°–82°N). The maximal BSII was 45% in 2016 which is the smallest value since the beginning of the record in 1979. Although the year 2016 was exceptionally low in terms of ice coverage, there is a suggestion of a regime shift in 2005: the BSII ranged between 70% and 100% before 2005 whereas it ranged between 45% and 78% from 2005 to 2022. Investigating marine heatwaves (MHW) in the Barents Sea from four decades of daily SST, Bayoumy et al. (2022) found that 2004 was a pivotal year, with amplified increasing SST trend (0.25°C/decade in the northern Barents Sea) and an increase in the annual mean MHW frequency and duration in the post-2004 period. We note that most of the previous studies we have compared our results with are based on observations prior to 2005. The hydrography of the Barents Sea is undergoing profound changes since the mid-2000s with an overall increase in temperature and salinity (Asbjørnsen et al., 2020; Barton et al., 2018; Lind et al., 2018; Oziel et al., 2016; Schlichtholz, 2019; Skagseth et al., 2020). These changes are a regional expression of the so-called "Atlantification" (Polyakov et al., 2017), associated with a reduced sea ice import and the disappearance of the fresher, colder surface water layer in the northwestern Barents Sea which sets conditions preventing sea ice formation (Lind et al., 2018). Warming and sea ice decline is particularly intensified in the northwestern Barents Sea, and primarily driven by horizontal advection of AW (Asbjørnsen et al., 2020; Schlichtholz, 2019). Here we further note that the dissolved oxygen concentration of the water conveyed by the CC, including MW in the upper 20 m, was relatively low (~315–325 μmol kg^{-1}), contrasting with the upper water in the fjord interior away from the Atlantic intrusion (~330–350 μmol kg^{-1}). This is consistent with an Atlantification of the water upstream of Storfjorden in the northwestern Barents Sea.

4.2. Overflow of BSW

BSW formed in the winter was found in the main depression of Storfjorden, as in many previous studies, but also, more anecdotally, in a secondary 105 m-deep depression at 78°15'N. The densest BSW had a salinity of 34.95 ($\sigma_\theta = 28.12$ kg m^{-3}) that is low compared with most prior observations, but not exceptionally so. The intriguing aspect of these observations is the dome of remnant BSW that peaked at a depth of 90 m, well above the sill level (~120 m), while there was no evidence of overflow of BSW at the sill. The velocity field clearly featured a closed cyclonic circulation centered on the depression (Figure 6a).

Flows over finite isolated topography have been an active subject of theoretical research (e.g., Huppert, 1975; Ingersoll, 1969; McCartney, 1975). For steep enough topography, a region of closed streamlines appears. This circulation pattern trapped above the obstacle is referred to as a Taylor column (Taylor, 1923). While the theories are often applied to seamounts, they also apply *mutatis mutandis* to flows over depressions, which is what interests us here. There has been a significant number of observations of stratified Taylor columns in the ocean (e.g., Brechner Owens & Hogg, 1980; Hogg, 1973), most, if not all, associated with a seamount. A more recent example, at high latitudes, is the warm-core anticyclonic circulation over Discovery Bank in the Southern Ocean (Meredith et al., 2015).

Ingersoll (1969) provided an analytical solution for a uniform retrograde (westward) flow of magnitude U over a flat cylinder of height h_0 for an homogeneous and inviscid layer of fluid of depth H in the f-plane approximation. With these hypotheses, closed streamlines (a Taylor column) appear when

$$h_0/H > 2R_o, \tag{1}$$

where $R_o = U/fL$ is the Rossby radius, L the horizontal scale of the obstacle and f the Coriolis parameter. Although the case of flow around a depression was not explicitly discussed by Ingersoll (1969), his analytical solution can be extended to the case of a cylindrical depression by taking a negative cylinder height (Huppert, 1975, footnote p. 401), which yields the expected cyclonic circulation. The Storfjorden depression is stretched in the meridional direction, with a width of ~50 km at 77°15'N (Figure 4) and meridional span of ~90 km (Figure 5). We crudely represent this depression as a cylindrical hole of height $h_0 = 70$ m and radius $R = 30$ km in an ocean of depth $H = 70$ m. With typical flows of 10 cm s^{-1} and $f = 1.42 \times 10^{-4}$ s^{-1}, the Rossby number is O (0.01) whereas the scaled depression depth is O (1) so that the condition (Equation 1) for the appearance of a Taylor column over the depression is satisfied. Huppert (1975) extended the work of Ingersoll (1969) to consider the additional effect of stratification. Stratification tends to confine the influence of topographic variations near the bottom, more specifically to a vertical scale of order $h_s = fL/N$, where $N = \sqrt{-g/\rho_0 \partial\rho/\partial z}$ is the Brunt-Väisälä frequency, g the gravitational acceleration, and ρ_0 the density of sea water. Here, N is on the order of 5×10^{-3} s^{-1}, increasing to 0.02–0.03 s^{-1} in the upper 20 m. This yields a vertical scale $h_s \approx$ 300–1,700 m, indicating that a Taylor column would extend from the bottom to the surface. To understand how a cyclonic barotropic flow rapidly induces a doming of isopycnals we refer to the study of Hill (1996). Using linearized quasi-geostrophic dynamics in a two-layer axisymmetric setting, his analysis demonstrated that, due to bottom friction, the circulation spins down in the lower layer within a time scale of a few days, ultimately confining the residual cyclonic circulation to the surface layer, above an up-domed interface. The velocity field of Figure 6a does show significant surface intensification, with near zero velocity below 120 m, consistent with the baroclinic flow induced by the doming. The study of Hill (1996), which showed that dense dome structures (with cyclonic surface circulation) can be expected to be static, is particularly relevant here as the geometry of the problem examined is almost exactly that encountered in Storfjorden.

The BSW thus appears to be maintained as a dome within a closed cyclonic circulation pattern consistent with a Taylor column. For a homogeneous fluid, the interior of the column would eventually come to rest (Ingersoll, 1969) whereas stratification limits the effect of bottom friction to the lower layers through a doming of isopycnals. External forcings (e.g., atmospheric forcing) may disrupt this dynamical equilibrium, leading to an episodic outflow. An episodic discharge regime is described to occur as of October (Skogseth, Haugan, & Jakobsson, 2005) whereas our observations were collected mid-July. Episodic discharge is reported to occur when the BSW reservoir has emptied down to the sill level, which was not the case in the present observations.

From their current meter time series from 2003 to 2007, Geyer et al. (2009) found that the variability of the overflow on the scale of 1–2 weeks is strongly connected to wind forcing. The suggested physical mechanism was

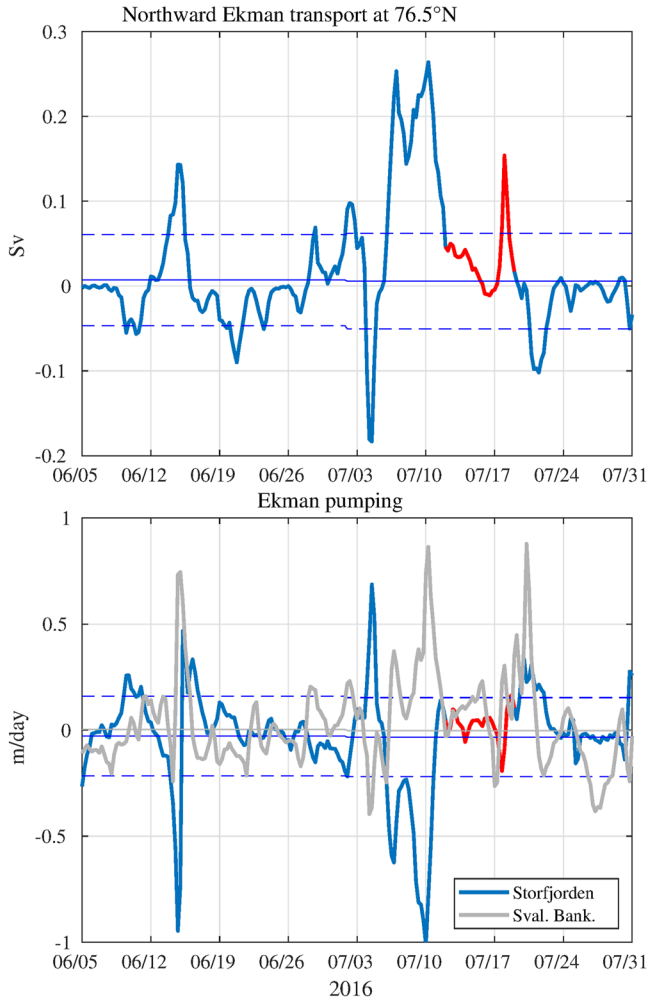

Figure 13. Top: Ekman transport into Storfjorden at 76.5°N integrated between 18°E and 21°E. The red segment denotes the span of the cruise. The monthly average and standard deviation of 6-hourly data from the monthly average are denoted by the solid and the dashed thin blue lines, respectively. Bottom: Ekman pumping velocity averaged in Storfjorden (blue) and over Storfjordrenna and Svalbardbanken (gray) between 17° and 30°E and 73°–76°N (unit in m day^{-1}).

that the surface Ekman transport into the fjord caused by northeasterly winds is balanced by a flow at depth at the Storfjorden sill. The dynamics discussed above provide further insight into the details of this mechanism: surface Ekman convergence into Storfjorden induces downwelling Ekman pumping velocity, which brings negative vorticity to the flow. This slows down the cyclonic circulation in Storfjorden by vortex squeezing, which acts against the maintenance of the observed dome shape for the BSW retained above the sill level. Another observed feature, which is the relationship between the intensity of the overflow and that of the coastal circulation, can be understood as well with the dynamical equilibrium described above. Skogseth, Haugan, and Jakobsson (2005) suggested that the BSW overflow is also compensated by the CC, with a stronger CC when the BSW overflow is small, as was the case in August 2001, and vice versa. Our observations yielding a transport estimate of 0.14 Sv for the CC (consistent with the outstanding 0.11 Sv of August 2001) together with the absence of overflow are consistent with their conclusion. An enhanced doming is indeed associated both with a stronger cyclonic circulation in the upper ocean and a reduced overflow.

Following Geyer et al. (2009), we have computed the Ekman transport into Storfjorden, denoted F_{Ek}, by zonally integrating the zonal wind stress τ_x along 76.5°N,

$$F_{Ek} = -\int_{18°E}^{21°E} \tau_x/(\rho_0 f)\, dx. \quad (2)$$

The time series of F_{Ek} during the summer 2016 is displayed in Figure 13 (top), jointly with the monthly average and monthly standard deviation of this parameter computed from 17 years of 6-hourly data (2002–2018). We have also computed the average Ekman pumping velocity over Storfjorden from the wind stress curl ($w_e = 1/\rho_0$ curl (τ/f)), forcing the wind stress τ at zero on land to mimic the convergence/divergence associated with the presence of a coast (Figure 13, bottom). It is apparent from these figures that the cruise occurred in the wake of a strongly anomalous Ekman flow into the fjord associated with intense northeasterlies, which started 6 July and lasted for about 5 days, reaching 0.26 Sv that is 4 times the July standard deviation. The downward Ekman pumping velocity for this period reached 1 m day^{-1}, consistent with the Ekman transport into Storfjorden (0.26 Sv translates to a vertical velocity of 1.46 m day^{-1} for a Storfjorden area of 15,000 km^2). According to the previous arguments, conditions were thus prone to a strong discharge episode a few days before the cruise. It is surprising not to have found remnants of an overflow at the section just south of the sill that was occupied about a week after this episode. Although it seems unlikely, we note, however, that with the observed O (0.05) cm s^{-1} bottom velocities there, the dense water may have moved ~30 km southward, that is just south of the section. Another possibility is that Ekman pumping was not strong enough to flatten the doming up to the point to trigger an overflow.

An intermittent discharge regime being unusual as early in the summer, another open question is whether a specific event/forcing generated in the first place the strong barotropic cyclonic circulation (Taylor column) that resulted in the observed doming. If so, it may be linked to the equally unusual intrusion of MAW into Storfjorden well north of the sill.

4.3. Flooding of Atlantic Waters

In the 2016 survey, Storfjorden was flooded with water of Atlantic origin spreading up to 78°N (e.g., Section 3.4) and the ArW reservoir of Storfjorden was entrapped by this northward migration of the PF (Section 3.3). It is difficult to assess, from the existing literature, how far north into Storfjorden water of Atlantic origin traditionally

reach, and how frequent such intrusions have been in the past. From 4 years of hydrographic data (1999–2002), Skogseth, Haugan, and Jakobsson (2005) stated that the presence of underlying NAW and MAW increases toward the sill and further southward and decreases northward and toward the coast, whereas the opposite is the case for ArW. In their schematic description of the Storfjorden-Storfjordrenna circulation, they referred to the channel south of the sill between the submarine ridge and Storfjordbanken where the PF is historically found (see also Schauer, 1995) as the "exchange zone." This zone is characterized by generally warmer and more saline water to the east resulting from a topographically guided inflow on the eastern side. In our observations, the exchange zone appeared to be stretched along most of the eastern side of Storfjorden, but also to the west of the meridional submarine ridge. Skogseth, Haugan, and Jakobsson (2005) clearly demonstrated the control exerted by the position of the PF on the abundance of the different water masses in Storfjorden and Storfjordrenna, with the volume of NAW and its by-products varying opposite to that of ArW, further adding "If NAW is strongly present, most likely the PF is situated along the northeastern part of Storfjordrenna as far north as to the sill." We have not found other discussions of the position of the PF in Storfjorden. To our knowledge, the intrusion of Atlantic waters into Storfjorden well north of the sill, with the concomitant entrapment of a pocket of ArW has been so far unreported.

By contrast, there has been numerous observations of intrusions of AW onto the West Spitsbergen Shelf and into the fjords of the west coast of Spitsbergen, in particular during winter, switching the hydrography from an Arctic to an Atlantic dominated system with reduced to non-existent sea ice (Cottier et al., 2007; Nilsen et al., 2008, 2016; Skogseth et al., 2020; Tverberg et al., 2019). The occurrence of these intrusions is reported to have increased during the recent decades in response to changes in the atmospheric circulation around Svalbard, especially regarding winter cyclones (Francis & Vavrus, 2012; Nilsen et al., 2016). Using a barotropic shelf circulation model, Nilsen et al. (2016) showed that the winter intrusions of AW are caused by strong southerly wind periods along the shelf with associated onshore Ekman transport that tends to increase the surface tilt over the shelf break, thus strengthening and widening the West Spitsbergen Current and forcing it to follow shallower isobaths.

Storfjorden is on the east coast of Spitsbergen and, therefore, has the opposite orientation with respect to the large scale wind forcing. At the same time, Storfjordrenna opens to the western shelf of Spitsbergen, so that the previous argument could be relevant to explain the MAW inflow in Storfjorden. A depression coming from the Greenland Sea associated with strong southwesterlies did hit Svalbard on 3 July 2016, inducing a sharp Ekman transport out of Storfjorden (Figure 13, top). However, this gale lasted less than 1 day, so that its influence in terms of forcing was probably moderate compared to the even stronger and much longer lasting northeasterlies that followed during 5–12 July. Note that it is unlikely that the large Ekman transport into the fjord caused by these strong northeasterlies is responsible for the AW intrusion. As already noted, the associated downwelling Ekman pumping velocity (Figure 13) brings negative vorticity to the flow, opposing the cyclonic circulation in Storfjorden. The reason for the PF migration into the fjord, instead, is likely to be non-local forcing, upstream of Storfjorden.

The gray line of Figure 13 (bottom) shows the average Ekman pumping velocity in the regions south of Storfjorden, between 17°–30°E and 73°–76°N, thus including Storfjordrenna and Svalbardbanken, but also part of Bear Island Trough. This region was chosen because it encompasses the pathway of the bundle of isobaths between 100 and 300 m upstream of Storfjorden, which go around Svalbardbanken: the PF is reported to follow the 150 m (Loeng, 1991) or 220 m isobath (Barton et al., 2018). Given the scale of atmospheric forcing, however, results are not very sensitive to the exact domain; fairly similar results are obtained for an average limited to 17°–23°E, or even for an average along 18°E following the pathway of the shelf break. While the wind stress curl is generally nearly zero over this region in summer, Figure 13 (bottom) shows a succession of positive anomalies in the 2 weeks preceding the cruise, four of which exceeding one standard deviation. The average Ekman pumping between 27 June and 11 July is 0.13 m day^{-1}, which is a very substantial 15-day long positive anomaly compared to the 17-year climatological average of -6×10^{-4} m day^{-1} over the same period (17-year standard deviation of 0.18 m day^{-1} for 6-hourly values and of 0.06 m day^{-1} for the 2-week averages). The unusual atmospheric forcing in the summer 2016 over the Barents Sea was pointed out by Bayoumy et al. (2022), a situation which they related to a positive Eastern Atlantic Pattern in summer 2016, following Chafik et al. (2017).

To understand how a positive wind stress curl anomaly could force the flow toward shallower depth we resort to barotropic dynamics, which also underpin the argument of Nilsen et al. (2016). For an inviscid homogeneous steady state ocean, neglecting nonlinear terms, the vorticity budget for the vertically integrated flow **u** over a depth H reduces to the topographic Sverdrup balance (e.g., Vivier et al., 2005, Appendix A)

$$\mathbf{u} \cdot \nabla \frac{f}{H} = \mathrm{curl}\left(\frac{\boldsymbol{\tau}}{\rho_0 H} \right). \quad (3)$$

In the absence of forcing, this simple equation states that the flow is constrained to follow f/H contours (Taylor-Proudman theorem). Considering wind forcing, Equation 3 shows that a positive wind stress curl anomaly induces a flow in the direction of the gradient of f/H, that is toward shallower depths in the northern hemisphere (over a region small enough to neglect the variations of f compared to those of H). We conclude that the observed positive wind stress curl anomaly over Svalbardbanken and Storfjordrenna set up conditions prone for a migration of the flow (i.e., a migration of the PF) toward shallower depth. Once a depth shallower than 120 m (the sill depth) has been reached, obstacles to the progression into Storfjorden are much diminished, similarly to what has happened along the West Spitsbergen Shelf (Skogseth et al., 2020).

Of course, even with a consistent dynamical argument, we cannot definitely pin down positive wind stress curl anomalies over Svalbardbanken as the cause of the PF migration into Storfjorden based on a single observation. One can also argue that the dynamics of the PF are more complex and cannot be reduced to a simple topographic Sverdrup balance. In this respect we refer to Gawarkiewicz and Plueddemann (1995), who showed that the flow of NAW in the Barents Sea is barotropic and linear, following the bathymetry. More recently Barton et al. (2018) have provided additional evidences that the PF in the Barents Sea is controlled by simple potential vorticity constraints. Other possible causes can also be invoked (which do not necessarily exclude the previous mechanism), beginning with an increased intensity of the NAC, which responds to the wind forcing at 55°N on the long time scales associated with baroclinic Rossby waves (Orvik & Skagseth, 2003). Using satellite altimetry, Oziel et al. (2020) have recently shown that the North Atlantic Current surface velocities have nearly doubled over the last 24 years.

4.4. Water Mass Transformation

The anomalous hydrography in Storfjorden in the summer 2016 was associated with significant differences in terms of water mass transformation compared with the available literature. The bottom plume leaving Storfjordrenna south of Sørkapp carried warm (1°C) PW rather than the expected cold water resulting from an overflow of BSW. For comparison, at this section, Schauer (1995) reported bottom temperature lower than −0.5°C in June 1991 and Fer et al. (2003) found −1.5°C in June 2001. The plume had a density of $\sigma_\theta = 27.94$ kg m^{-3}, which is too light, even if not mixed en route, to sink underneath the AW layer in the Fram Strait limited by the $\sigma_\theta = 27.97$ kg m^{-3} isopycnal (Rudels et al., 2005), and thus feed the Arctic Ocean intermediate or deep waters reservoir. Moreover its volume transport was 0.02 Sv, which is only about 20% of the values reported in the literature. Indeed Schauer (1995) found 0.13 Sv in 1992, Fer et al. (2003) reported 0.12 Sv in 2001, whereas Jungclaus et al. (1995) estimated 0.11 Sv from a numerical simulation. The denser water found entering Storfjordrenna from the southwest had a density of 27.87 kg m^{-3}, lighter than the water exiting with the PW plume, indicating nonetheless water mass transformation along the Storfjorden-Storfjordrenna circuit.

We have already discussed the absence, during the 2016 cruise, of a BSW overflow as traditionally defined at the sill ($\sigma_\theta \geq 28.05$ kg m^{-3}, Skogseth, Haugan, & Jakobsson, 2005), possibly as the consequence of the establishment of an intermittent discharge regime anomalously early in the season. The densest water found just south of the sill in the middle of the trough had a density of 28.00 kg m^{-3} but a temperature well above the freezing point (∼−1°C), indicating mixing of BSW with ESW. Skogseth, Haugan, and Jakobsson (2005) considered this mixture as the upper layer of the BSW overflow. In the 2016 survey, there was no lower layer and the southward transport of this densest layer was only 0.002 Sv, far less than the 0.06 Sv reported by Fer et al. (2003) in 2001. The distribution of water masses at the bottom was contrasted between the western slope of the trough south of the sill, occupied by cold ArW, and that to the east where outflowing ESW was found. The bottom outflow to the west was found at 115 m, near the sill depth, and characterized by a temperature close to the freezing point (−1.59°C). With a salinity of 34.77, lower than the 34.8 characterizing BSW, it is classified as ArW, although most likely formed similarly except for a lesser ice formation/brine release. Note that, in the earlier literature on the subject, BSW is defined using only a temperature criterion. Based on the criterion $\theta < -1.5$°C, Schauer (1995) found that a small fraction (<3%) of the BSW sampled in their 1 year long current meter record had a density within the range of typical AW densities (<27.95 kg m^{-3}) corresponding to BSW salinities between 34.50 and 34.73. Relaxing the BSW definition as above does not appear relevant here as this comprises only a narrow water column

segment at 19°E in a depth range of 80–120 m, shallower than the sill (Figure 7, bottom). We can, nevertheless, quantify the production of dense water in Storfjorden using the criterion $\sigma_\theta \geq 27.95$ kg m^{-3} which captures most of the outflowing water on the western slope (Figure 10c). The corresponding southward flow of 0.034 Sv that extends from 80 m to the bottom over the western slope has a mean density of $\sigma_\theta = 27.975$ kg m^{-3}, a mean temperature of −0.9°C and a mean salinity of 34.78.

A peculiarity of the observations from summer 2016 is the evidence of formation of ESW within Storfjorden. ESW was identified by Quadfasel et al. (1988) at stations west of Hopenbanken, hence upstream of Storfjorden. Skogseth, Haugan, and Jakobsson (2005) discussed the formation of ESW south of the sill (a layer apparent as a salinity minimum above the Storfjorden overflow) which results from the mixing of ArW with PW and BSW, a mixing induced by the overflow. In the 2016 data we find no inflow of ESW into Storfjorden, which was instead formed locally as is supported by the outflow apparent south of the sill (Figure 9, bottom). Observations suggest that it predominantly results from the isopycnal mixing of ArW and PW. The higher density of ESW compared to PW or NAW (Figure 3; right) is due to cabbeling. Cabbeling refers to convection induced by the effect of contraction on mixing with a nonlinear equation of state (Foster, 1972). While cabbeling is limited by vertical static stability, and instead replaced by double diffusive convection when parent water masses lie one above the other (McDougall, 1981), it is an effective process for horizontally adjacent water masses as is the case here. Likewise, cabbeling was found to be an active process at the Arctic Front on the West Spitsbergen Shelf (Cottier & Venables, 2007). Finding ESW and denser PW forming in Storfjorden is a consequence of the displacement of the PF north of sill, which appears to have transformed Storfjorden into a more regular extension of Storfjordrenna. These ESW and dense PW contributed about 0.01 Sv, 0.004 Sv of which had a $\sigma_\theta \geq 27.95$ kg m^{-3} and were included in the previous outflow estimate of 0.034 Sv. These estimates are based on a single hydrographic section and are therefore a snapshot in time.

5. Summary and Conclusion

The network of CTD-LADCP sections performed during the STEP cruise in July 2016 provided a comprehensive picture of the circulation and water masses transformation in the Storfjorden-Storfjordrenna system. The cruise occurred during a summer marked by an abnormal wind situation and following a winter season characterized by the lowest ice coverage in the Barents Sea over the entire 40-year long satellite record (with an ice break-up in Storfjorden 42 days in advance), and amid a regime shift that started in 2005 characterized by an Atlantification of the Barents Sea reported by many authors (e.g., Lind et al., 2018). These observations revealed striking differences with respect to previous studies that were mostly based on observations obtained prior to 2005.

A first notable difference was the near absence of SSW, at least with its known characteristics before 2005, which is usually the most abundant water mass in the upper 60 m of Storfjorden in summer (e.g., Haarpaintner, O'Dwyer, et al., 2001). In 2016, this was replaced by a saltier water mass ($0 < \theta \leq 4.0$°C; $34.4 < S < 34.8$), that seems to be ArW that has warmed without mixing with fresh MW. Consistent with this interpretation, MW was absent in summer 2016 over most of Storfjorden except at the periphery where it is brought about by the cyclonic CC (also known as Sørkapp Current or Spitsbergen Polar Current). The transport of the latter measured during the cruise was 0.14 Sv which is, to our knowledge, the first direct estimate.

Another remarkable aspect of these observations was the flooding of Storfjorden with water of Atlantic origin spreading up to 78°N and the associated entrapment of the ArW reservoir of Storfjorden by the northward migration of the PF along the eastern flank of the fjord, far north of the sill. The juxtaposition of the two water masses promoted isopycnal mixing and the local formation of ESW and denser PW in the fjord through cabbeling instability. The origin of this intrusion is not completely established, but it may have been favored by a sequence of positive wind stress curl anomalies over Svalbardbanken (Spitsbergen bank) and Storfjordrenna in the few weeks preceding the cruise (Figure 13, bottom), forcing the NAW /MAW to follow shallower isobaths, that is, causing the migration of the PF toward shallower depths, which enabled to pass the sill.

Remnant BSW was found in the depression of Storfjorden. The densest BSW had a salinity of 34.95 ($\sigma_\theta = 28.12$ kg m^{-3}) which is fresh compared with previous reports, but not exceptionally so. A striking and intriguing aspect of these observations was the dome of BSW that reached up to a depth of 90 m, well above the 120 m sill level, while there was no evidence of a gravity driven overflow of BSW south of the sill. This dome-like shape associated with a 0.15 Sv cyclonic circulation is consistent with a stratified Taylor column locked over

the depression (bottom friction generates an uplift of isopycnal toward the center of the column as demonstrated by Hill (1996)). The cruise occurred a few days after a 5-day long episode of intense northeasterlies that generated strongly anomalous Ekman flow into the fjord reaching 0.26 Sv, conditions that are prone to boost the overflow (Geyer et al., 2009). It is possible that the absence of overflow during the cruise was due to a relapse after a strong discharge episode. An intermittent discharge regime is typical of October, once the BSW reservoir has drained down to the sill level (Skogseth, Haugan, & Jakobsson, 2005) and would, therefore, be very unusual this early in the summer. Another hypothesis is that the anomalous Ekman pumping was not strong enough to slow down the cyclonic circulation to the point where the overflow would trigger, which raises the question of the generation of a strong cyclonic circulation in the first place. We speculate that the latter could be remotely forced, following the mechanism suggested for the intrusion of NAW into the fjord.

A weak (0.02 Sv) bottom plume was found leaving Storfjordrenna south of Sørkapp. It carried relatively warm (1°C) PW rather than the expected cold water resulting from an overflow of BSW. With a density of $\sigma_\theta = 27.94$ kg m^{-3}, it was too light to sink underneath the Atlantic layer in the Fram Strait. The densest NAW sampled entering Storfjordrenna from the southwest had a density of 27.87 kg m^{-3}, lighter than the densest water exiting (PW), indicating nonetheless water mass transformation along the Storfjorden-Storfjordrenna circuit. While there was no evidence of a gravity driven overflow south of the sill, characterized in the literature by the layer $\sigma_\theta \geq 28.05$ kg m^{-3} (Skogseth, Haugan, & Jakobsson, 2005), the outflow of water denser than $\sigma_\theta = 27.95$ kg m^{-3} was 0.034 Sv, 10% of which was contributed by ESW formed in Storfjorden north of the sill, which is unusual based on previously reported observations. Isopycnal mixing of ArW and MAW generated another 0.006 Sv of a slightly lighter class of dense water composed of ESW and the densest PW.

Given the predictions of declining ice cover in the Arctic, especially in the Eurasian basin, one could conjecture that these observations, made in the wake of an exceptional 2015–2016 winter season, prefigure what the average summer hydrographic conditions in Storfjorden could be in the near future. However, while some of the observed changes appear to involve a preconditioning during the previous low-sea-ice winter, others appear to be related to anomalous wind forcing in the weeks preceding the cruise. Assessing to what extent these changes are to be considered a new hydrographic state of Storfjorden requires further observations.

Data Availability Statement

Hydrographic and current velocity data from the STEP cruise are available from the French oceanographic data center SEANOE at https://doi.org/10.17882/86706.

Acknowledgments
The STEP campaign was supported by the French Oceanographic Fleet (FOF). We gratefully acknowledge support from CNRS INSU (LEFE program), and in particular its Technical Division. We thank the crew and captain of R/V *L'Atalante*. Maps have been drawn with the M_Map Matlab toolbox (Pawlowicz, 2020). We thank the two anonymous reviewers and Editor Laurence Padman whose comments and recommendations have enabled to substantially improve the initial manuscript. We dedicate this work to our late colleague and delightful friend Nicolas Martin who should have been on board with us.

References

Aagaard, K. (1981). On the deep circulation in the Arctic Ocean. *Deep Sea Research Part A: Oceanographic Research Papers*, *28*(3), 251–268. https://doi.org/10.1016/0198-0149(81)90066-2

Aagaard, K., Swift, J. H., & Carmack, E. C. (1985). Thermohaline circulation in the Arctic Mediterranean seas. *Journal of Geophysical Research*, *90*(C3), 4833–4846. https://doi.org/10.1029/JC090iC03p04833

Akimova, A., Schauer, U., Danilov, S., & Núñez-Riboni, I. (2011). The role of the deep mixing in the Storfjorden shelf water plume. *Deep Sea Research Part I: Oceanographic Research Papers*, *58*(4), 403–414. https://doi.org/10.1016/j.dsr.2011.02.001

Anderson, L. G., Falck, E., Jones, E. P., Jutterstrom, S., & Swift, J. H. (2004). Enhanced uptake of atmospheric CO_2 during freezing of seawater: A field study in Storfjorden, Svalbard. *Journal of Geophysical Research*, *109*(C6), C06004. https://doi.org/10.1029/2003JC002120

Anderson, L. G., Peter Jones, E., Lindegren, R., Rudels, B., & Sehlstedt, P.-I. (1988). Nutrient regeneration in cold, high salinity bottom water of the Arctic shelves. *Continental Shelf Research*, *8*(12), 1345–1355. https://doi.org/10.1016/0278-4343(88)90044-1

Asbjørnsen, H., Årthun, M., Skagseth, O., & Eldevik, T. (2020). Mechanisms underlying recent Arctic atlantification. *Geophysical Research Letters*, *47*(15), e2020GL088036. https://doi.org/10.1029/2020GL088036

Barton, B. I., Lenn, Y.-D., & Lique, C. (2018). Observed Atlantification of the Barents Sea causes the Polar Front to limit the expansion of winter sea ice. *Journal of Physical Oceanography*, *48*(8), 1849–1866. https://doi.org/10.1175/JPO-D-18-0003.1

Bayoumy, M., Nilsen, F., & Skogseth, R. (2022). Marine heatwaves characteristics in the Barents Sea based on high resolution satellite data (1982–2020). *Frontiers in Marine Science*, *9*, 4436. https://doi.org/10.3389/fmars.2022.821646

Bensi, M., Kovačević, V., Langone, L., Aliani, S., Ursella, L., Goszczko, I., et al. (2019). Deep flow variability offshore south-west Svalbard (Fram Strait). *Water*, *11*(4), 683. https://doi.org/10.3390/w11040683

Brechner Owens, W., & Hogg, N. G. (1980). Oceanic observations of stratified Taylor columns near a bump. Deep Sea Research Part A. *Oceanographic Research Papers*, *27*(12), 1029–1045. https://doi.org/10.1016/0198-0149(80)90063-1

Chafik, L., Nilsen, J. E., & Dangendorf, S. (2017). Impact of North Atlantic teleconnection patterns on northern European sea level. *Journal of Marine Science and Engineering*, *5*(3), 43. https://doi.org/10.3390/jmse5030043

Cottier, F. R., Nilsen, F., Inall, M. E., Gerland, S., Tverberg, V., & Svendsen, H. (2007). Wintertime warming of an Arctic shelf in response to large-scale atmospheric circulation. *Geophysical Research Letters*, *34*(10), L10607. https://doi.org/10.1029/2007GL029948

Cottier, F. R., & Venables, E. J. (2007). On the double-diffusive and cabbeling environment of the Arctic front, West Spitsbergen. *Polar Research*, *26*(2), 152–159. https://doi.org/10.3402/polar.v26i2.6222

Dee, D. P., Uppala, S. M., Simmons, A. J., Berrisford, P., Poli, P., Kobayashi, S., et al. (2011). The ERA-interim reanalysis: Configuration and performance of the data assimilation system. *Quarterly Journal of the Royal Meteorological Society*, *137*(656), 553–597. https://doi.org/10.1002/qj.828

D'Errico, J. (2006). *Surface fitting using gridfit*. MATLAB Central File Exchange.

Egbert, G. D., & Erofeeva, S. Y. (2002). Efficient inverse modeling of barotropic ocean tides. *Journal of Atmospheric and Oceanic Technology*, *19*(2), 183–204. https://doi.org/10.1175/1520-0426(2002)019⟨0183:EIMOBO⟩2.0.CO;2

Fer, I., & Ådlandsvik, B. (2008). Descent and mixing of the overflow plume from Storfjord in Svalbard: An idealized numerical model study. *Ocean Science*, *4*(2), 115–132. https://doi.org/10.5194/os-4-115-2008

Fer, I., Skogseth, R., & Haugan, P. M. (2004). Mixing of the Storfjorden overflow (Svalbard Archipelago) inferred from density overturns. *Journal of Geophysical Research*, *109*(C1), C01005. https://doi.org/10.1029/2003JC001968

Fer, I., Skogseth, R., & Jaccard, P. (2003). Observations of the Storfjorden overflow. *Deep-Sea Research*, *50*(10–11), 1283–1303. https://doi.org/10.1016/S0967-0637(03)00124-9

Foster, T. D. (1972). An analysis of the cabbeling instability in sea water. *Journal of Physical Oceanography*, 2(3), 294–301. https://doi.org/10.1175/1520-0485(1972)002⟨0294:AAOTCI⟩2.0.CO;2

Francis, J. A., & Vavrus, S. J. (2012). Evidence linking Arctic amplification to extreme weather in mid-latitudes. *Geophysical Research Letters*, *39*(6), L06801. https://doi.org/10.1029/2012GL051000

Gawarkiewicz, G., & Plueddemann, A. J. (1995). Topographic control of thermohaline frontal structure in the Barents Sea polar front on the south flank of Spitsbergen Bank. *Journal of Geophysical Research*, *100*(C3), 4509–4524. https://doi.org/10.1029/94JC02427

Geyer, F., Fer, I., & Eldevik, T. (2009). Dense overflow from an Arctic fjord: Mean seasonal cycle, variability and wind influence. *Continental Shelf Research*, *29*(17), 2110–2121. https://doi.org/10.1016/j.csr.2009.08.003

Grasshoff, K., Ehrhardt, M., & Kremling, K. (1983). *Methods of seawater analysis* (2nd ed., p. 420). Verlag Chemie.

Haarpaintner, J. (1999). The Storfjorden polynya: ERS-2 SAR observations and overview. *Polar Research*, *18*(2), 175–182. https://doi.org/10.1111/j.1751-8369.1999.tb00290.x

Haarpaintner, J., Gascard, J.-C., & Haugan, P. M. (2001). Ice production and brine formation in Storfjorden, Svalbard. *Journal of Geophysical Research*, *106*(C7), 1–13. https://doi.org/10.1029/1999JC000133

Haarpaintner, J., O'Dwyer, J., Gascard, J.-C., Haugan, P. M., Schauer, U., & Østerhus, S. (2001). Seasonal transformation of water masses, circulation and brine formation observed in Storfjorden, Svalbard. *Annals of Glaciology*, *33*, 437–443. https://doi.org/10.3189/172756401781818635

Helland-Hansen, B., & Nansen, F. (1909). The Norwegian Sea: Its physical oceanography based upon the Norwegian Researches 1900–1904. *Report on Norwegian Fishery and Marine Investigations* (Vol. 2(2), p. 359). Available online at http://hdl.handle.net/11250/114874

Hill, A. E. (1996). Spin-down and the dynamics of dense pool gyres in shallow seas. *Journal of Marine Research*, *54*(3), 471–486. https://doi.org/10.1357/0022240963213538

Hoerl, A., & Kennard, R. (1970). Ridge regression: Biased estimation for nonorthogonal problems. *Technometrics*, *12*(1), 55–67. https://doi.org/10.1080/00401706.1970.10488634

Hogg, N. G. (1973). The preconditioning phase of MEDOC 1969—II. Topographic effects. *Deep-Sea Research and Oceanographic Abstracts*, *20*(5), 449–459. https://doi.org/10.1016/0011-7471(73)90099-5

Huppert, H. E. (1975). Some remarks on the initiation of inertial Taylor columns. *Journal of Fluid Mechanics*, *67*(2), 397–412. https://doi.org/10.1017/S0022112075000377

Ingersoll, A. P. (1969). Inertial Taylor columns and Jupiter's great red spot. *Journal of the Atmospheric Sciences*, *26*(4), 744–752. https://doi.org/10.1175/1520-0469(1969)026⟨0744:ITCAJG⟩2.0.CO;2

Iwamoto, K., Ohshima, K. I., & Tamura, T. (2014). Improved mapping of sea ice production in the Arctic Ocean using AMSR-E thin ice thickness algorithm. *Journal of Geophysical Research*, *119*(6), 3574–3594. https://doi.org/10.1002/2013JC009749

Jardon, F., Vivier, F., Lourenço, A., Bouruet-Aubertot, P., Cuypers, Y., & Willmes, S. (2014). Ice production in Storfjorden (Svalbard) estimated from a simple model based on AMSR-E observations: Impact on water mass properties. *Journal of Geophysical Research*, *119*(1), 377–393. https://doi.org/10.1002/2013JC009322

Jungclaus, J. H., Backhaus, J. O., & Fohrmann, H. (1995). Outflow of dense water from the Storfjord in Svalbard: A numerical model study. *Journal of Geophysical Research*, *100*(C12), 24719–24728. https://doi.org/10.1029/95JC02357

Le Bot, P., Kermabon, C., Lherminier, P., & Gaillard, F. (2011). CASCADE v6.1: Logiciel de validation et de visualisation des mesures ADCP de coque. Rapport technique OPS/LPO 11-01 (Tech. Rep.). Ifremer, Centre de Brest.

Lind, S., Ingvaldsen, R., & Furevik, T. (2018). Arctic warming hotspot in the northern Barents Sea linked to declining sea-ice import. *Nature Climate Change*, *8*(7), 634–639. https://doi.org/10.1038/s41558-018-0205-y

Loeng, H. (1991). Features of the physical oceanographic conditions of the Barents Sea. *Polar Research*, *10*(1), 5–18. https://doi.org/10.3402/polar.v10i1.6723

Maus, S. (2003). Interannual variability of dense shelf water salinities in the north-Western Barents Sea. *Polar Research*, *22*(1), 59–66. https://doi.org/10.3402/polar.v22i1.6444

McCartney, M. S. (1975). Inertial Taylor columns on a beta plane. *Journal of Fluid Mechanics*, *68*(1), 71–95. https://doi.org/10.1017/S0022112075000699

McDougall, T. J. (1981). Double-diffusive convection with a nonlinear equation of state: Part II. Laboratory experiments and their interpretation. *Progress in Oceanography*, *10*(2), 91–121. https://doi.org/10.1016/0079-6611(81)90002-1

McDougall, T. J., & Barker, P. M. (2011). *Getting started with TEOS-10 and the Gibbs seawater (GSW) oceanographic toolbox* (p. 28). SCOR/IAPSO WG127. ISBN 978-0-646-55621-5.

Meredith, M. P., Meijers, A. S., Naveira Garabato, A. C., Brown, P. J., Venables, H. J., Abrahamsen, E. P., et al. (2015). Circulation, retention, and mixing of waters within the Weddell-Scotia confluence, Southern Ocean: The role of stratified Taylor columns. *Journal of Geophysical Research: Oceans*, *120*(1), 547–562. https://doi.org/10.1002/2014JC010462

Michel, E., & Vivier, F. (2016). STEP 2016 cruise, RV L'Atalante. https://doi.org/10.17600/16000900

Midttun, L. (1985). formation of dense bottom water in the Barents Sea. Deep Sea Research Part A. *Oceanographic Research Papers*, *32*(10), 1233–1241. https://doi.org/10.1016/0198-0149(85)90006-8

Nansen, F. (1906). *Northern waters: Captain Roald Amundsen's oceanographic observations in the Arctic seas in 1901*. In I. Videnskabs-Selskabets SkrifterI (Ed.) (Vol. 3, p. 145). Mathematisk-Naturv. Klasse.

Nilsen, F., Cottier, F., Skogseth, R., & Mattsson, S. (2008). Fjord–shelf exchanges controlled by ice and brine production: The interannual variation of Atlantic Water in Isfjorden, Svalbard. *Continental Shelf Research*, *28*(14), 1838–1853. https://doi.org/10.1016/j.csr.2008.04.015

Nilsen, F., Skogseth, R., Vaardal-Lunde, J., & Inall, M. (2016). A simple shelf circulation model: Intrusion of Atlantic Water on the West Spitsbergen shelf. *Journal of Physical Oceanography*, *46*(4), 1209–1230. https://doi.org/10.1175/JPO-D-15-0058.1

Orvik, K. A., & Skagseth, O. (2003). The impact of the wind stress curl in the North Atlantic on the Atlantic inflow to the Norwegian Sea toward the Arctic. *Geophysical Research Letters*, *30*(17), 1884. https://doi.org/10.1029/2003GL017932

Oziel, L., Baudena, A., Ardyna, M., Massicotte, P., Randelhoff, A., Sallée, J.-B., et al. (2020). Faster Atlantic currents drive poleward expansion of temperate phytoplankton in the Arctic Ocean. *Nature Communications*, *11*(1), 1705. https://doi.org/10.1038/s41467-020-15485-5

Oziel, L., Sirven, J., & Gascard, J.-C. (2016). The Barents Sea frontal zones and water masses variability (1980–2011). *Ocean Science*, *12*(1), 169–184. https://doi.org/10.5194/os-12-169-2016

Padman, L., & Erofeeva, S. (2004). A barotropic inverse tidal model for the Arctic Ocean. *Geophysical Research Letters*, *31*(2), L02303. https://doi.org/10.1029/2003GL019003

Pawlowicz, R. (2020). M_map: A mapping package for Matlab. (version 1.4m), [Computer software]. EOAS. Available online at www.eoas.ubc.ca/~rich/map.html

Piechura, J. (1996). Dense bottom waters in Storfjord and Storfjordrenna. *Oceanologia*, *38*(2), 285–292.

Polyakov, I. V., Pnyushkov, A. V., Alkire, M. B., Ashik, I. M., Baumann, T. M., Carmack, E. C., et al. (2017). Greater role for Atlantic inflows on sea-ice loss in the Eurasian Basin of the Arctic Ocean. *Science*, *356*(6335), 285–291. https://doi.org/10.1126/science.aai8204

Preußer, A., Willmes, S., Heinemann, G., & Paul, S. (2015). Thin-ice dynamics and ice production in the Storfjorden polynya for winter seasons 2002/2003–2013/2014 using MODIS thermal infrared imagery. *The Cryosphere*, *9*(3), 1063–1073. https://doi.org/10.5194/tc-9-1063-2015

Quadfasel, D., Rudels, B., & Kurz, K. (1988). Outflow of dense water from a Svalbard fjord into the Fram Strait. *Deep-Sea Research, Part A: Oceanographic Research Papers*, *35*(7), 1143–1150. https://doi.org/10.1016/0198-0149(88)90006-4

Rousset, C., Vancoppenolle, M., Madec, G., Fichefet, T., Flavoni, S., Barthélemy, A., et al. (2015). The Louvain-La-Neuve sea-ice model LIM3.6: Global and regional capabilities. *Geoscientific Model Development*, *8*(10), 2991–3005. Special Issue: Nucleus for European Modelling of the Ocean—NEMO. https://doi.org/10.5194/gmd-8-2991-2015

Rudels, B. (1986). The θ-S relations in the northern seas: Implications for the deep circulation. *Polar Research*, *4*(2), 133–159. https://doi.org/10.1111/j.1751-8369.1986.tb00527.x

Rudels, B., Björk, G., Nilsson, J., Winsor, P., Lake, I., & Nohr, C. (2005). The interaction between waters from the Arctic Ocean and the Nordic seas north of Fram Strait and along the East Greenland current: Results from the Arctic Ocean-02 Oden expedition. *Journal of Marine Systems*, *55*(1), 1–30. https://doi.org/10.1016/j.jmarsys.2004.06.008

Rudels, B., & Quadfasel, D. (1991). Convection and deep water formation in the Arctic Ocean-Greenland Sea System. *Journal of Marine Systems*, *2*(3), 435–450. https://doi.org/10.1016/0924-7963(91)90045-V

Sanchez-Vidal, A., Veres, O., Langone, L., Ferré, B., Calafat, A., Canals, M., et al. (2015). Particle sources and downward fluxes in the eastern Fram strait under the influence of the west Spitsbergen current. *Deep Sea Research Part I: Oceanographic Research Papers*, *103*, 49–63. https://doi.org/10.1016/j.dsr.2015.06.002

Schauer, U. (1995). The release of brine-enriched shelf water from Storfjord into the Norwegian Sea. *Journal of Geophysical Research*, *100*(C8), 16015–16028. https://doi.org/10.1029/95JC01184

Schauer, U., & Fahrbach, E. (1999). A dense bottom water plume in the Western Barents Sea: Downstream modification and interannual variability. *Deep-Sea Research*, *46*(12), 2095–2108. https://doi.org/10.1016/S0967-0637(99)00046-1

Schlichtholz, P. (2019). Subsurface ocean flywheel of coupled climate variability in the Barents Sea hotspot of global warming. *Scientific Reports*, *9*(1), 13692. https://doi.org/10.1038/s41598-019-49965-6

Skagseth, Ø., Eldevik, T., Årthun, M., Asbjørnsen, H., Lien, V. S., & Smedsrud, L.-H. (2020). Reduced efficiency of the Barents Sea cooling machine. *Nature Climate Change*, *10*(7), 661–666. https://doi.org/10.1038/s41558-020-0772-6

Skogseth, R., Fer, I., & Haugan, P. M. (2005a). Dense-water production and overflow from an Arctic coastal polynya in Storfjorden. In H. Drange, T. Dokken, T. Furevik, R. Gerdes, & W. Berger (Eds.), *The Nordic seas: An integrated perspective-oceanography, climatology, biogeochemistry, and modeling*. American Geophysical Union. https://doi.org/10.1029/158GM07

Skogseth, R., Haugan, P., & Haarpaintner, J. (2004). Ice and brine production in Storfjorden from four winters of satellite and in situ observations and modeling. *Journal of Geophysical Research*, *109*(C10), C10008. https://doi.org/10.1029/2004JC002384

Skogseth, R., Haugan, P. M., & Jakobsson, M. (2005b). Watermass transformations in Storfjorden. *Continental Shelf Research*, *25*(5), 667–695. https://doi.org/10.1016/j.csr.2004.10.005

Skogseth, R., Olivier, L., Nilsen, F., Falck, E., Fraser, N., Tverberg, V., et al. (2020). Variability and decadal trends in the Isfjorden (Svalbard) Ocean climate and circulation—An indicator for climate change in the European Arctic. *Progress in Oceanography*, *187*, 102394. https://doi.org/10.1016/j.pocean.2020.102394

Skogseth, R., Smedsrud, L. H., Nilsen, F., & Fer, I. (2008). Observations of hydrography and downflow of brine-enriched Shelf water in the Storfjorden polynya, Svalbard. *Journal of Geophysical Research*, *113*(C8), C08049. https://doi.org/10.1029/2007JC004452

Smith, W. H. F., & Sandwell, D. T. (1997). Global seafloor topography from satellite altimetry and ship topo soundings. *Science*, *277*, 1957–1962.

Spreen, G., Kaleschke, L., & Heygster, G. (2008). Sea ice remote sensing using AMSR-E 89 Ghz channels. *Journal of Geophysical Research*, *113*(C2), C02S03. https://doi.org/10.1029/2005JC003384

Swift, J. H., Takahashi, T., & Livingston, H. D. (1983). The contribution of the Greenland and Barents seas to the deep water of the Arctic Ocean. *Journal of Geophysical Research*, *88*(C10), 5981–5986. https://doi.org/10.1029/JC088iC10p05981

Taylor, G. I. (1923). Experiments on the motion of solid bodies in rotating fluids. In *Proceedings of the Royal Society A* (Vol. 106, pp. 213–218).

Thurnherr, A. M. (2014). How to process LADCP data with the LDEO software (versions 9.7—9.10). *Computer software manual*.

Tverberg, V., Skogseth, R., Cottier, F., Sundfjord, A., Walczowski, W., Inall, M., et al. (2019). In H. Hop & C. Weincke (Eds.), *The Kongsfjorden transect: Seasonal and inter-annual variability in hydrography*. The Ecosystem of Kongsfjorden.

Vivier, F., Kelly, K. A., & Harismendy, M. (2005). Causes of large-scale sea level variations in the Southern Ocean: Analyses of sea level and a barotropic model. *Journal of Geophysical Research*, *110*(C9), C09014. https://doi.org/10.1029/2004JC002773

Wobus, F., Shapiro, G. I., Huthnance, J. M., Morales Maqueda, M. A., & Aksenov, Y. (2013). Tidally induced lateral dispersion of the Storfjorden overflow plume. *Ocean Science*, *9*(5), 885–899. https://doi.org/10.5194/os-9-885-2013